Towards soil moisture profile estimation in the root zone using L- and P-band radiometer observations: A coherent modelling approach

Foad Brakhasi, Jeffrey Walker, Nan Ye, Xiaoling Wu, Xiaoji Shen, In-Young Yeo, Nithyapriya Boopathi, Edward Kim, Yann H. Kerr, Thomas Jackson

Towards soil moisture profile estimation in the root zone using L- and P-band radiometer observations: A coherent modelling approach

Foad Brakhasi, Jeffrey P. Walker, Nan Ye, Xiaoling Wu, Xiaoji Shen, In-Young Yeo, Nithyapriya Boopathi, Edward Kim, Yann Kerr, Thomas Jackson

PII: S2666-0172(23)00004-4

DOI: https://doi.org/10.1016/j.srs.2023.100079

Reference: SRS 100079

To appear in: *Science of Remote Sensing*

Received Date: 18 November 2022

Revised Date: 11 February 2023

Accepted Date: 20 February 2023

Please cite this article as: Brakhasi, F., Walker, J.P., Ye, N., Wu, X., Shen, X., Yeo, I.-Y., Boopathi, N., Kim, E., Kerr, Y., Jackson, T., Towards soil moisture profile estimation in the root zone using L- and P-band radiometer observations: A coherent modelling approach, *Science of Remote Sensing* (2023), doi: https://doi.org/10.1016/j.srs.2023.100079.

Towards soil moisture profile estimation in the root zone using L- and P-band radiometer observations: A coherent modelling approach

Foad Brakhasi [a, *], Jeffrey P. Walker[a], Nan Ye [a], Xiaoling Wu[a], Xiaoji Shen[a, b], In-Young Yeo[c], Nithyapriya Boopathi[d], Edward Kim[e], Yann Kerr[f], and Thomas Jackson[g]

[a] Department of Civil Engineering, Monash University, Clayton, Australia

[b] Yangtze Institute for Conservation and Development, Hohai University, Nanjing, China

[c] School of Engineering, The University of Newcastle, Callaghan, Australia

[d] IITB-Monash Research Academy, Mumbai, India

[e] NASA Goddard Space Flight Center, Greenbelt, USA

[f] Centre d'Etudes Spatiales de la Biosphère, Toulouse, France

[g] USDA ARS Hydrology and Remote Sensing Laboratory (Retired), Beltsville, USA

[*] *Corresponding author.*

E-mail addresses: foad.brakhasi@monash.edu, brakhasi.f@gmail.com.

ABSTRACT

Precision irrigation management and crop water stress assessment rely on accurate estimation of root zone soil moisture. However, only the top 5 cm soil moisture can be estimated using the two current passive microwave satellite missions, Soil Moisture and Ocean Salinity (SMOS) and Soil Moisture Active Passive (SMAP), which operate at L-band (wavelength of ~21 cm). Since the contributing depth of the soil to brightness temperature increases with observation wavelength, it is expected that a P-band (wavelength of ~40 cm) radiometer could potentially provide soil moisture information from deeper layers of the soil profile. Moreover, by combining both L- and P- bands, it is hypothesized that the soil moisture profile can be estimated even beyond their individual observation depths. The aim of this study was to demonstrate the potential of combined L-band and P-band radiometer observations to estimate the soil moisture profile under flat bare soil using a stratified coherent forward model. Brightness temperature observations at L-band and P-band from a tower based experimental site across a dry (April 2019) and a wet (March 2020) period, covering different soil moisture profile shapes, were used in this study. Results from an initial synthetic study showed that the performance of a combined L-band and P-band approach was better than the performance of using either band individually, with an average depth over which reliable soil moisture profile information could be estimated (i.e. with a target root mean square error (RMSE) of less than 0.04 m^3/m^3) being 20 cm for linear and 15 cm for second-order polynomial functions. Other functions were also tested but found to have a poorer performance. Applying the method to the tower-based brightness temperature achieved an average estimation depth of 28 cm (20 cm) and 5 cm (5 cm) during the dry and wet periods respectively when using a second-order polynomial (linear) function. These findings highlight the opportunity of a satellite mission with L-band and P-band observations to accurately estimate the soil moisture profile to as deep as 30cm globally.

Keywords: Soil moisture profile estimation, Coherent model, Multi-frequency, L-band, P-band, Passive microwave

1. Introduction

Soil moisture is a key state variable in the water, energy, and carbon cycles (Falloon et al., 2011; Zhang et al., 2019). While soil moisture accounts for only a small fraction of the freshwater globally (0.15%), it has an important impact on rainfall-runoff processes (Brocca et al., 2012), regulates net ecosystem exchange (Chu et al., 2019), constrains food security (Sadri et al., 2020), and influences land-atmosphere interactions (Yuan et al., 2020). However, many studies have shown large variability in the spatial and temporal distribution of soil moisture, especially in the top 20 cm of the soil (Shi et al., 2014), emphasizing the necessity of monitoring these variations. Moisture in this region of the soil profile limits the plant's photosynthetic activity and transpiration (Seneviratne et al., 2010; Reich et al., 2018). In addition, information on the root zone soil moisture is used for irrigation scheduling (Liang et al., 2016), understanding of plant stress and pesticide management (Malone et al., 2004; Jiang et al., 2021). As compared to estimation of moisture in the shallow layer, root zone soil moisture estimation is more challenging (Etminan et al., 2020). Accurate spatial and periodic mapping of this vital variable through direct measurement is almost impossible due to its cost-intensive and time-consuming measurement, higher spatio-temporal variability, and non-linear relationship with surface soil moisture (Das and Mohanty, 2006; Sabater et al., 2007; Hu and Si, 2014; Gao et al., 2019).

Microwave remote sensing techniques have been identified as the most promising approach for global observation of near-surface soil moisture content (Karthikeyan et al., 2017). Specifically, passive microwave remote sensing at L-band has been widely adopted with current remote sensing satellites dedicated to the monitoring of soil moisture, including the European Space Agency (ESA) Soil Moisture and Ocean Salinity (SMOS; Kerr et al., 2010)

and the National Aeronautics and Space Agency (NASA) Soil Moisture Active Passive (SMAP; Entekhabi et al., 2014) missions. While L-band can observe a deeper layer of soil than shorter wavelengths, its soil moisture measurement is limited to just a few centimeters of the soil (Zheng et al., 2019; Shen et al., 2020, 2022a). Therefore, researchers have investigated different techniques for estimating the root zone soil moisture from surface soil moisture including multiple regression (Qiu et al., 2010; Mahmood et al., 2012), data assimilation (Walker et al., 2001; Baldwin et al., 2017), and statistical/empirical methods such as machine learning (Carranza et al., 2021; Karthikeyan and Mishra, 2021; Xia et al., 2022), principle of maximum entropy (Mishra et al., 2018; Zhou et al., 2016), and exponential filters (Mishra et al., 2020). The approach chosen is usually based on the application, level of complexities involved and the amount of a priori information available. When it comes to applications on a large scale, the number of inputs needed is of utmost importance, especially in areas where data is scarce. As a result, approaches that require minimal inputs have gained attention in these types of applications. Generally, all the models require establishing a relationship between surface and root-zone soil moisture. However, the relationship between the two is often nonlinear and becomes weaker with depth, making it challenging to capture using conventional statistical techniques (Ford et al., 2014).

The multiple regression models are simple and relatively straightforward to interpret, but they have limitations in handling complex non-linear relationships between input and output variables. These models are also sensitive to outliers, which means that even a small number of extreme values can significantly affect the results. Conversely, machine learning algorithms are well-suited to handle non-linear relationships between inputs and outputs, making them suitable for modeling complex soil moisture patterns. However, they require large amounts of training data to produce accurate estimates, which can be difficult to obtain in some cases. Additionally, some machine learning algorithms can be difficult to interpret, making it

challenging to understand the physical basis for their predictions and to identify areas for improvement. There is also a risk of overfitting, where the algorithm becomes too specialized to the training data and does not generalize well to new data. The principle of maximum entropy method does not rely on prior information about the profile, but it requires the values of surface soil moisture, the average moisture content, and the moisture content of the bottom-most layer, which are difficult to obtain. The exponential filter only requires the time series of surface soil moisture, which is easily available from microwave sensors, however sensitivity is reduced during prolonged dry periods and in deeper layers where plant uptake is the main factor affecting root-zone moisture movement due to the assumption of no transpiration and constant hydraulic conductivity.

Current regional or global scale root zone soil moisture products such as Soil Moisture Ocean Salinity (SMOS) level 4 RZSM data, Soil Moisture Active Passive (SMAP) level 4 RZSM data, the Japanese 55-year Reanalysis (JRA-55), National Centers for Environmental Prediction (NCEP) Reanalysis version 1 (NCEP R1) and 2 (NCEP R2), the Modern-Era Retrospective analysis for Research and Applications, Version 2 (MERRA-2), the fifth generation European Centre for Medium-Range Weather Forecasts (ECMWF) atmospheric reanalysis (ERA-5), and the Global Land Data Assimilation System (GLDAS) are based on assimilation of surface soil moisture into land surface models (LSMs) or global hydrological models (GHMs) (Xu et al., 2021). The Ensemble Kalman Filter is a widely used assimilation algorithm in land surface models, but its implementation is claimed to be inappropriate because of non-linear relationships between observations and model states (Clark et al., 2008).

Compared with L-band (1.4 GHz; 5cm sensing depth), P-band (750 MHz) has been shown to be more sensitive to soil moisture over deeper layers (~10 cm; Shen et al., 2020). As the L-band and P-band emissions are derived from different depths in the soil (Shen et al., 2020), there is the potential to derive insights into the depth variation of soil moisture by using the

two together. Some researchers have used P-band radar alone (Tabatabaeenejad et al., 2013, 2015, 2016, 2017; Sadeghi et al., 2016; Chen et al., 2018; Etminan et al., 2020; Yueh et al., 2020) or combined with L-band radar (Du et al., 2015; Chen et al., 2016, 2017; Azemati et al., 2019; Yi et al., 2019) to estimate root zone soil moisture. While their results have shown the concept to be promising, they have typically applied constraints, been limited to snapshot retrieval, and been applied to radar rather than radiometer observations. Moreover, a comprehensive investigation of the different mathematical functions that might be used to represent the soil moisture profile is lacking. Importantly, compared with a radiometer, radar is more sensitive to vegetation and surface roughness (Engman and Chauhan, 1995), and thus it is possible that multi-frequency L-and P-band radiometer observations could provide more accurate soil moisture profile estimation than that obtained from radar.

The aim of this research was to study the use of multi-frequency (L- and P-band) radiometry to estimate the root zone profile for flat bare soil. The forward stratified coherent model of Njoku and Kong (1977) was applied to calculate brightness temperature (TB) from soil moisture and temperature profiles. While the coherent and incoherent models have the same general trend, the former includes phase-interference oscillations (Ulaby and Long, 2014). The main differences between them relate to the effects of interference, which is a function of frequency and the steepness of soil moisture profile near the surface (Schmugge and Choudhury, 1981). When data from regions of rapid sub-surface moisture variations (rapid drying out or a region having a subsurface water table) are interpreted with depth, the incoherent models become inaccurate, since coherent reflections are not accounted for. Also, when there is considerable diurnal surface temperature variation, incoherent models become inaccurate for longer wavelengths. Thus, the coherent models of Njoku and Kong (1977) and Wilheit (1978) were introduced and formulated in terms of continuous and discrete varying dielectric constant within the soil, respectively. Only a small difference was observed between

the Njoku and Wilheit models (Schmugge and Choudhury, 1981) and so in this research the Njoku model was used.

The analysis has considered single or dual-frequency, single or dual-polarization, single or multi-incidence angle, and snapshot or time series retrieval options. Several mathematical functions have been investigated as representative functions of the soil moisture profile, namely i) Linear (hereafter Li), ii) Exponential (Exp), iii) Second-order Polynomial (Pn2), iv) simplified solution of the Richards' Equation (RE), v) Parametrized second-order polynomial from the simplified solution of the Richards' Equation (PRE), vi) Third-order Polynomial (Pn3), and vii) Piecewise Linear (PL).

2. Data

As part of the P-band Radiometer Inferred Soil Moisture project (PRISM; www.prism.monash.edu), a comprehensive tower-based experiment site was established at Cora Lynn, Victoria, Australia from October 2017 to September 2021 to advance the state of microwave remote sensing technology readiness (Fig. 1). The tower was instrumented with the Polarimetric P-band Multi-beam Radiometer (PPMR) and the Polarimetric L-band Multi-beam Radiometer (PLMR), operating at 0.742-0.752 GHz and 1.400-1.425 GHz, respectively. The tower was located at the center of 4 quadrants, each with a size of 75 m × 75 m, in order to observe different land cover conditions but similar soil moisture status (Shen et al., 2020). The PPMR has a phased array antenna with four beams having 30° beamwidth, distributed at angles of ±15° and ±45° from the normal to the antenna plane, and the PLMR has six antenna beams having 15° beamwidth distributed at angles ±7.5°, ±21°, and ±38.5° from the normal to the antenna plane. These radiometers could not only be rotated in azimuth to look at the different quadrants but tilted to change the look angles, which was done automatically according to a predefined schedule. Footprints of PLMR and PPMR for two extreme incidence angles of 30° and 60° are shown in Fig. 1. At the middle border of each quadrant ground stations (called

stations 126, 127, 128 and 136) were installed, equipped with hydra-probes that simultaneously measured the soil moisture and temperature from the soil surface to 60 cm depth at 5 cm intervals. Soil texture analysis was also conducted for different locations and depths, providing an average (standard deviation, depth 5cm, depth 20 cm, depth 50 cm) soil texture of 18.3% (± 3.15%, 18%, 17%, 17%) clay, 13.7% (± 5.89%, 12%, 11%, 20%) sand, and 68% (± 5.12%,

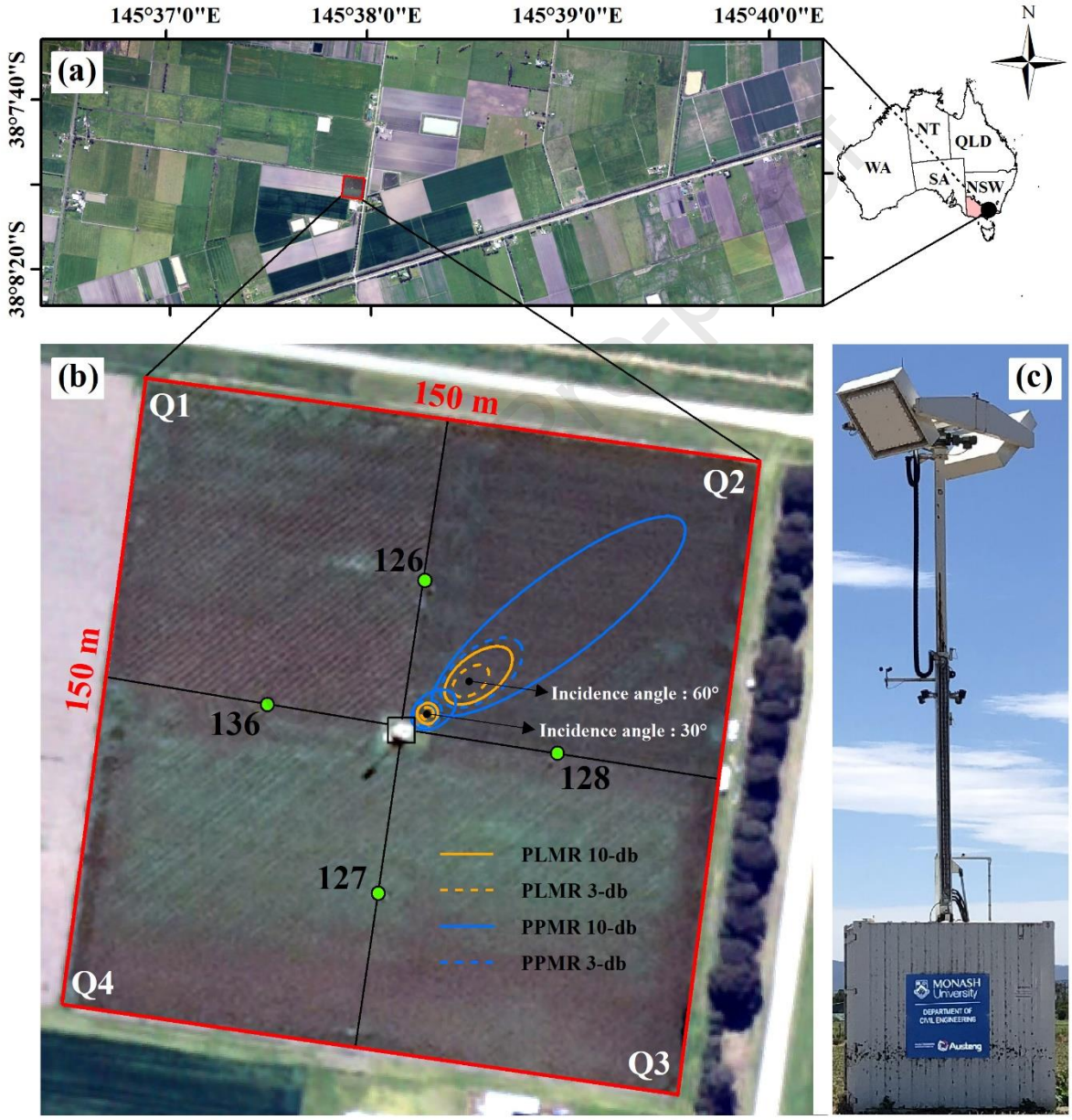

Fig. 1. Location map (a) of the experimental site (b) having a tower (c) at the center of a paddock at Cora Lynn, Victoria, Australia. The colored ovals represent the footprints of the microwave radiometers. The green dots represent the stations installed at the borders of the quadrants Q1 to Q4.

186 71%, 69%, 62%) silt, indicating a silty loam soil. The quadrants were maintained under
187 different conditions in terms of vegetation type (corn, wheat, grass or bare) and surface
188 roughness (smooth, furrow and bench furrow with parallel or perpendicular row orientation;
189 (Shen et al., 2022b)). For simplicity, this research has focused on the flat bare soil condition.
190 The performance of a multi-frequency optimization approach was investigated using
191 experimental data of soil moisture and temperature profiles from the soil surface to 60 cm depth

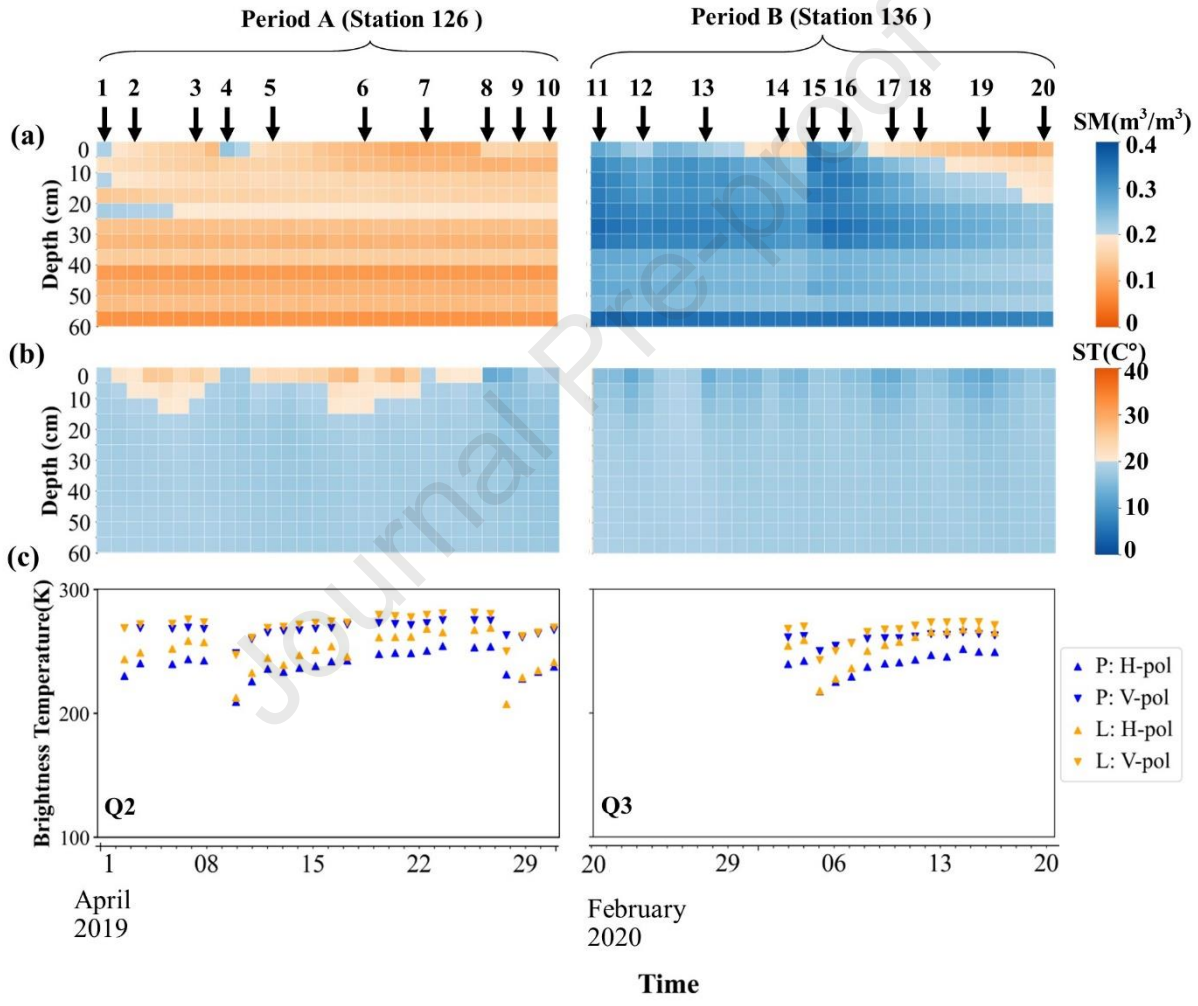

Fig. 2. Evolution time series of (a) soil moisture and (b) soil temperature as a function of depth were measured at Cora Lynn station number 126 (period A) and 136 (period B), and (c) brightness temperature from PPMR and PLMR at quadrant 2 over Period A (1st - 30th April 2019) and quadrant 3 over Period B (20th February to 20th March 2020). The twenty black arrows show the timing of the soil moisture and temperature profiles used for snapshot and time series retrieval in the synthetic study.

in 5 cm increments, covering soil moisture conditions ranging from 0.07 to 0.35 m3/m3. Data from stations 126 and 136 as shown in Fig. 2 (a and b), and tower-based TB as shown in Fig. 2 (c), were used under flat and bare soil conditions for two periods, namely A (1st to 30th April, 2019) and B (20th February to 20th March, 2020). Fig. 2 (a and b) shows the high variability of moisture and temperature in the near-surface layer relative to deeper layers in the profile. It is seen during Period A that variation of soil moisture in the deeper layers was much lower than Period B, with high variability of moisture in almost all of the soil layers. Despite rapid drying of the surface and shallow layers, the deeper layers of the soil were slow to respond (see soil moisture at deeper layers in Fig. 2 (a)). Compared to soil moisture, soil temperature has a

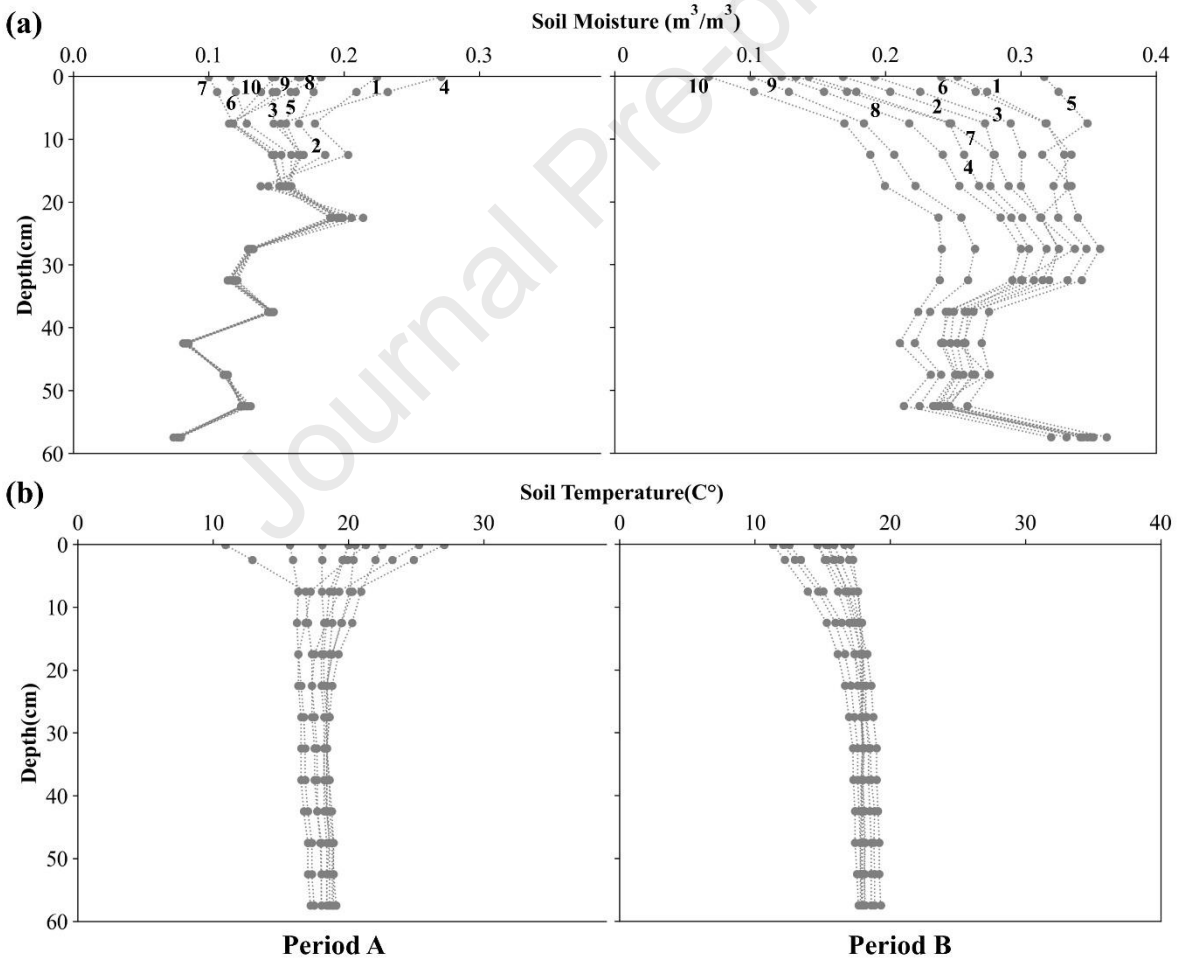

Fig. 3. Selected (a) soil moisture and (b) temperature profiles for this research. All of these soil moisture profiles were used in investigating different mathematical functions to represent the soil moisture and soil temperature profile.

strong day to day variation and cooling of the near-surface layer relative to deeper layers for Period A compared with Period B (Fig. 2 (c)).

In an initial synthetic study, the twenty soil moisture and soil temperature profiles in Fig. 3, selected from the two periods in Fig. 2 to cover the different profile shapes identified in Fig. 4, were used to predict TB values for developing the soil moisture profile estimation process. The selected data were used for answering questions including: i) if single or multi-frequency provide better results; ; ii) if single or multi-incidence angles yield better results; iii) if single (H or V) or dual (H and V) polarization provide a more robust solution; iv) which mathematical function(s) provides the best results; v) whether a snapshot or time series approach performs best; and vi) the impact of soil temperature profile approximation on the soil moisture profile estimation accuracy?

3. Methodology

Quantification of soil moisture using passive microwave remote sensing relies on a model, which in its simplest form can be a regression model, or in its most complex form a physical model. Microwave emission models are physical models that take the form of either a coherent or an incoherent model for soil moisture estimation. In this research, the coherent stratified model of Njoku and Kong (1977) was employed.

3.1 Forward model background

A vertically inhomogeneous half-space model (Njoku and Kong, 1977), hereafter referred to as the Njoku model, was used as the forward model to simulate TB at the sensor level. The theory behind such an approach uses electromagnetic fluctuations and electromagnetic wave propagation as formulated by Stogryn (1970), which established a relationship between emitted energy and the properties of the medium (surface roughness, soil moisture, and physical

224 temperature). Mathematically, TB at H (Eq.1) and V (Eq.2) polarization from the Njoku model
225 is written as:

$$TB_H = \frac{k}{cos\theta}\int_{-\infty}^{0} dzT(z)\,\epsilon_r{}''(z)|\psi(z)|^2 \tag{1}$$

$$TB_V = \frac{1}{kcos\theta}\int_{-\infty}^{0} dzT(z)\,\epsilon_r{}''(z).\left\{\left|\frac{1}{\epsilon_r(z)}\,\frac{d\phi(z)}{d(z)}\right|^2 + \left|\frac{k_x\phi(z)}{\epsilon_r(z)}\right|^2\right\}, \tag{2}$$

226 where $K = \frac{2\pi}{\lambda}$ is the free space wave number, $k_x = k\sin\theta$, θ is the angle of observation,
227 $\epsilon_r(z) = \epsilon_r'(z) + i\epsilon_r{}''(z)$ is the complex dielectric constant profile, and $T(z)$ is the soil
228 temperature profile. The functions $\psi(z)$ and $\phi(z)$ are solutions of the following two second-
229 order differential equations (Eq.3 and Eq.4):

$$\left\{\frac{d\psi(z)}{dz} + ikcos\theta[2-\psi(z)]\right\}_{z=0} = 0 \tag{3}$$

$$\left\{\frac{d\phi(z)}{dz} + i\epsilon_r(z)kcos\theta[2-\phi(z)]\right\}_{z=0} = 0. \tag{4}$$

230 These wave propagation equations are solved in conjunction with the boundary condition for a
231 smooth surface. From the perspective that at lower frequencies more information about soil
232 moisture comes from the deeper layers of the soil, Tsang et al. (1975) reformulated Eq.1 and
233 Eq.2 for a large number of horizontal layers. This was then incorporated by Njoku and Kong
234 (1977) and referred to as a stratified medium approach for smooth and bare soil according to
235 Eq.5 (for H polarization) and Eq.6 (for V polarization):

$$TB_H = \frac{k}{cos\theta}\sum_{l=1}^{N}\frac{\epsilon_l^{"}T_l}{\epsilon_0}\Bigg(\frac{|A_l\,exp(-ik_{lz}\,d_l)|^2}{2k_lz^{"}}\{1-exp\big[2k_lz^{"}(d_{l-1}-d_l)\big]\} \tag{5}$$

$$-\frac{|B_l\,exp(-ik_{lz}\,d_l)|^2}{2k_lz^{"}}\{1-exp\big[-2k_lz^{"}(d_{l-1}-d_l)\big]\}$$

$$-\left(\frac{[A_l\,exp(-ik_{lz}\,d_l)][B_l\,exp(-ik_{lz}\,d_l)]^*}{2ik_lz'}\right)\{1$$

$$-exp[-i2k_{lz}{}'(d_{l-1}-d_l)]\}$$

$$+\left(\frac{[A_l\,exp(-ik_{lz}\,d_l)]*[B_l\,exp(-ik_{lz}\,d_l)]}{2ik_lz'}\right)\{1$$

$$-exp[-i2k_{lz}{}'(d_{l-1}-d_l)]\}\Bigg)+\frac{k}{cos\theta}\frac{\epsilon_t^{"}T_t}{\epsilon_0}\frac{|T_h|^2\exp(-2k_{tz}{}^{"}d_n)}{2k_tz^{"}}$$

$$TB_V = \frac{k}{cos\theta}\sum_{l=1}^{N}\frac{\epsilon_l^{"}T_l}{\epsilon_0|k_l|^2}\,\big(|k_{lz}|^2 \tag{6}$$

$$+k_x{}^2\Big)\Bigg[\frac{|C_l\,exp(-ik_{lz}\,d_l)|^2}{2k_lz^{"}}\{1-exp\big[-2k_lz^{"}(d_l-d_{l-1})\big]\}$$

$$-\frac{|D_l\,exp(ik_{lz}\,d_l)|^2}{2k_lz^{"}}\{1-exp\big[2k_lz^{"}(d_l-d_{l-1})\big]\}$$

$$+\frac{|k_{lz}|^2-k_x{}^2}{|k_{lz}|^2+k_x{}^2}\Bigg(\frac{[C_l\,exp(-ik_{lz}\,d_l)][D_l\,exp(-ik_{lz}\,d_l)]^*}{2ik_lz'}\{1$$

$$-exp[-i2k_{lz}{}'(d_l-d_{l-1})]\}$$

$$-\frac{[C_l\,exp(-ik_{lz}\,d_l)]*[D_l\,exp(ik_{lz}\,d_l)]}{2ik_lz'}\{1$$

$$-exp[-i2k_{lz}{}'(d_l-d_{l-1})]\}\Bigg)\Bigg]$$

$$+\frac{k}{cos\theta}\frac{\epsilon_t^{"}\big(|k_{tz}|^2+k_x{}^2\big)T_t}{\epsilon_0|k_t|^2}|T_v|^2\frac{\exp(-2k_{tz}{}^{"}d_n)}{2k_{tz}{}^{"}},$$

where θ is the incidence angle, index l is the ID of the layer, $k=\frac{2\pi}{\lambda}=\omega\sqrt{\mu_0}\epsilon_0$ is the wavenumber in free space (λ is the wavelength, ω is the frequency in radiance/sec, μ_0 is the

permeability of free space, ϵ_0 is the permittivity of free space), $\epsilon_l = \epsilon_l' + i\epsilon_l''$ is the complex permittivity of the l^{th} layer, $\frac{\epsilon_l}{\epsilon_0}$ is the dielectric constant of l^{th} layer, T_l is the temperature in the l^{th} layer, $k_l = \omega\sqrt{\mu_0\epsilon_l}$ is the wavenumber in the l^{th} layer, $k_{lz} = k_{lz}{}' + ik_{lz}{}'' = k\sqrt{\epsilon_l/\epsilon_0 - sin^2\theta}$, d_l is the depth below the surface, and n is the total number of horizontal layers. The quantities A_l, B_l, C_l, D_l, T_h and T_v are wave amplitudes that are related to each other by propagation matrices. The impact of surface roughness was considered based on a semi-empirical approach (referred here to as the HQN model) which was proposed by (Wang and Choudhury, 1981) and developed by (Wigneron et al., 2001) through Eq.7.

$$r_{GP}(\theta) = \left[\left(1 - q_P(\theta)\right)r^*{}_{GP}(\theta) + q_P(\theta)r^*{}_{GQ}(\theta)\right] exp\left(-h_P(\theta)cos^{n_P}(\theta)\right), \tag{7}$$

where q_P (with $P = H$ and Q=V or $P = V$ and Q=H) is a polarization mixing factor, h_P is a surface roughness parameter, and n_P is the angular dependence of the surface roughness. The parameter h_P was calculated using (Wigneron et al., 2001) by Eq.8:

$$h_P = 1.3972 * \left(\frac{rms}{lc}\right)^{0.5879}, \tag{8}$$

where rms and lc are the RMS height and correlation length measured at the field for the two study periods. The parameter q_P was set to 0 for both L- and P- bands. The parameter n_P was calibrated using Eq.7 and the Njoku model from another period of data, yielding values of -0.50 (1.80) and -0.333 (0.415) at H (V) polarizations for L-band and P-band respectively. The parameter $r^*{}_{GP}$ is the specular reflectivity calculated from the Fresnel equations for H (Eq.9) and V (Eq.10) polarizations such that:

$$r^*{}_{GH} = \left|\frac{\cos(\theta) - \sqrt{\varepsilon_r - \sin^2(\theta)}}{\cos(\theta) + \sqrt{\varepsilon_r - \sin^2(\theta)}}\right|^2 \tag{9}$$

$$r^*{}_{GV} = \left|\frac{\varepsilon_r \cdot \cos(\theta) - \sqrt{\varepsilon_r - \sin^2(\theta)}}{\varepsilon_r \cdot \cos(\theta) + \sqrt{\varepsilon_r - \sin^2(\theta)}}\right|^2, \tag{10}$$

where $\varepsilon_r = \varepsilon_r' - i \cdot \varepsilon_r''$ is the relative soil dielectric constant which includes real ($'$) and imaginary ($''$) parts, and θ is the incidence angle. Using the coherent model, the emissivity is calculated in each layer, so by adjusting the calculated surface layer emissivity for roughness before multiplying by the physical temperature, the roughness can be included in the overall TB estimate by summing the TB contributions from each layer. Using the stratified coherent model to calculate the TB, with inputs of soil moisture and temperature, requires selecting an appropriate soil dielectric model, profile depth and a number of horizontal layers (profile depth divided by layer thickness). Here the multi-relaxation generalized refractive mixing dielectric model (Mironov et al., 2013, 2014) was used, as it considers the interfacial (Maxwell-Wagner) relaxation of water in the soil, which is significant at P band (Zhang et al., 2020). Schmugge and Choudhury (1981) recommended there be a total of 100 layers in 1 m profile depth (layer thickness varies from 0.003 cm at the surface to 1 cm at a depth of 9 cm and 5 cm at a depth of 40 cm) for 1.4 GHz frequency and higher. However, based on a sensitivity analysis using a combination of synthesized soil moisture and temperature profiles at various incidence angles using L- and P-band and H/V polarization, the profile depth and the number of horizontal layers did not exceed 0.9 m and 56 (when the layer thickness was 0.016). However, for preventing error from the numerical configuration of the model, they were set to 1 m and 0.01 m respectively, with 100 layers.

3.2 Mathematical representation of soil moisture and temperature profile

Several mathematical functions including Li (Eq.11), Exp (Eq.12), Pn2 (Eq.13), Pn3 (Eq.14), PL (Eq.15), RE (Eq.16) and PRE (Eq.21) were selected from literature (Reutov and Shutko, 1986; Tabatabaeenejad et al., 2015; Cuenca et al., 2016). Mathematically these functions are:

$$\mathrm{SM}(z) = az + c \tag{11}$$

$$\mathrm{SM}(z) = c + b(\exp(-az) - 1)/(\exp(-az_1) - 1) \tag{12}$$

$$\mathrm{SM}(z) = az^2 + bz + c \quad (13)$$

$$\mathrm{SM}(z) = az^3 + bz^2 + dz + c \quad (14)$$

$$\mathrm{SM}(z) = c + az + b(z - z_1)\mathrm{x}, \quad (15)$$

where z is depth (positive downward) and a, b, c and d are coefficients of the related function. Table 1 shows the boundaries of each parameter. The parameters a in Eq.11 and Eq.15 represent the profile slope of soil moisture content, while in Eq.12 and Eq.13 along with d in Eq.14 control the shape of the profile. Parameter b in Eq.12 is the change of moisture from the surface to the depth z_1 (0.6 m in this study), while in Eq.15 its value along with the a parameter is the slope of the second piece of the piecewise linear function. The parameter c in Eq.11 to Eq.15 represents the surface soil moisture content. Parameter z_1 in Eq.12 is the depth after which the soil moisture can be considered constant, while Eq.15 contains two linear segments that join at the depth z_1. Moreover, the binary vector x in Eq.15 is mathematically written as: if (z <=z_1,0,1). Notably, each of these functions has different computational requirements and degrees of complexity for fitting the shape variables. For example, the linear function has only two shape variables, while the exponential and second-order polynomial functions have three

Table 1. The boundaries of parameters used in the mathematical functions. SP (Shape Parameter; unitless), SSM (Surface Soil Moisture; % in Equations 12, m3/m3 in the rest), and ΔSM (the change of moisture in the profile from surface to the bottom of the profile (here 60 cm); %). The numbers in the brackets show the boundary [lower, upper] of each parameter.

Equation	***a***	***b***	***c***	***d***
11	Slope [-0.83, 0.83]	-	SSM [0, 0.5]	-
12	SP [-50, 50]	ΔSM [-35, 35]	SSM [0, 50]	-
13	SP [-1, 1]	SP [-1, 1]	SSM [0, 0.5]	-
14	SP [-1, 1]	SP [-1, 1]	SSM [0, 0.5]	SP [-1, 1]
15	Slope [-1, 1]	Slope [-1, 1]	SSM [0, 0.5]	-

shape variables, and the third-order polynomial and piecewise linear each have four shape variables. The simplified solution to Richards' equation Eq.16 has five parameters, two of which are empirical parameters (h_{cM} and P) related to effective capillary drive and soil pore size distribution respectively, given for different soils in Table 1 (51.64 and 10.84 respectively for the silty loam soil used here) of Sadeghi et al. (2016), while the rest (a, b, and c) are parameters controlling the shape of the profile and do not have any physical meaning. Consequently, these were parametrized according to the value of soil moisture at the top (θ_1), middle (θ_2), and bottom (θ_3) of the investigated depth (z_1, z_2 and z_3) as follows (Sadeghi et al., 2016):

$$\mathrm{SM}(z) = (az + b\exp\left(\frac{z}{h_{cM}}\right) + c)^{\frac{1}{P}} \tag{16}$$

$$a = \frac{\theta_3^P - \theta_1^P - A(\theta_2^P - \theta_1^P)}{z_3 - z_1 - A(z_2 - z_1)} \tag{17}$$

$$b = \frac{\theta_2^P - \theta_1^P - a(z_2 - z_1)}{\exp\left(\frac{z_2}{h_{cM}}\right) - \exp\left(\frac{z_1}{h_{cM}}\right)} \tag{18}$$

$$c = \theta_1^P - az_1 - bexp\left(\frac{z_1}{h_{cM}}\right) \tag{19}$$

$$A = \frac{\exp\left(\frac{z_3}{h_{cM}}\right) - \exp\left(\frac{z_1}{h_{cM}}\right)}{\exp\left(\frac{z_2}{h_{cM}}\right) - \exp\left(\frac{z_1}{h_{cM}}\right)}. \tag{20}$$

Assuming $P = 1$ and/or h_{cM} is larger than the investigation domain ($\frac{z}{h_{cM}} < 1$) leads to a second-order polynomial approximation (Eq.21):

$$\mathrm{SM}(z) = az + b\exp\left(\frac{z}{h_{cM}}\right) + c. \tag{21}$$

It is worth noting that the unknown parameters of Eq.16 and Eq.21 include the soil moisture value at the surface, middle, and bottom of the soil profile (0, 30 and 60 cm in the application here). When $P > 1$, and $\theta_1 < \theta_2 < \theta_3$ or $\theta_1 > \theta_2 < \theta_3$, the calculated soil moisture profile using

Eq.16 is undefined for a part of the profile. To solve this problem, P is considered as 1 so that the second-order polynomial in Eq.21 can be used.

Data throughout the period December 2017 to December 2019, having different wetting and/or drying regimes, was used to identify typical profile shapes and analyze the seven mathematical functions identified from literature for approximating soil profile conditions. This step was undertaken to aid in estimating the root zone soil moisture profile, as estimating a few shape parameters is a simpler task than estimating directly the soil moisture at multiple depths in the soil. The profile types (or shapes) are distinguished by changes in their moisture gradient, and their dynamic response to precipitation, evapotranspiration, soil properties etc. Type 1 in Fig. 4 (a) is a soil moisture profile that has little variation with depth (gradient or slope which can be decreasing, stable, or increasing). Type 2 in Fig. 4 (b) is a dry case with higher soil moisture at depth due to exfiltration. Type 3 in Fig. 4 (c) occurs when rain has wetted the soil near the surface and this has moved down through the soil column as plug flow, resulting in a sharp gradient neat the bottom of the profile. It could also happen if there are large differences in the soil texture such that the shallow layer can hold the moisture while the bottom of the profile does not. Type 4 in Fig. 4 (d) is where infiltration has occurred (due to rainfall) on the profile of Type 1, such that the profile takes a concave shape. Type 5 in Fig. 4 (e) is the most complex, taking on a S shape likely due to alternate wetting and drying cycles, resulting in substantial moisture variation throughout the profile. Samples of observed soil moisture profiles along with a typical soil temperature profile and their comparison with the fitted functions are illustrated in Fig. 4.

From the analysis it was concluded that depending on the time of the year, site, and its soil texture and infiltration dynamics, a mathematical function with a higher number of parameters will typically represent the soil moisture profile more accurately. The average RMSE (from surface to 60 cm depth) between soil moisture profiles from the fitted function and observed

328 soil moisture profiles were 0.026 (PL), 0.028 (Pn3), 0.03 (Pn2 and PRE), 0.032 (Exp), 0.034
329 (RE), and 0.035 (Li) (the unite is m^3/m^3). However, the greater number of parameters also

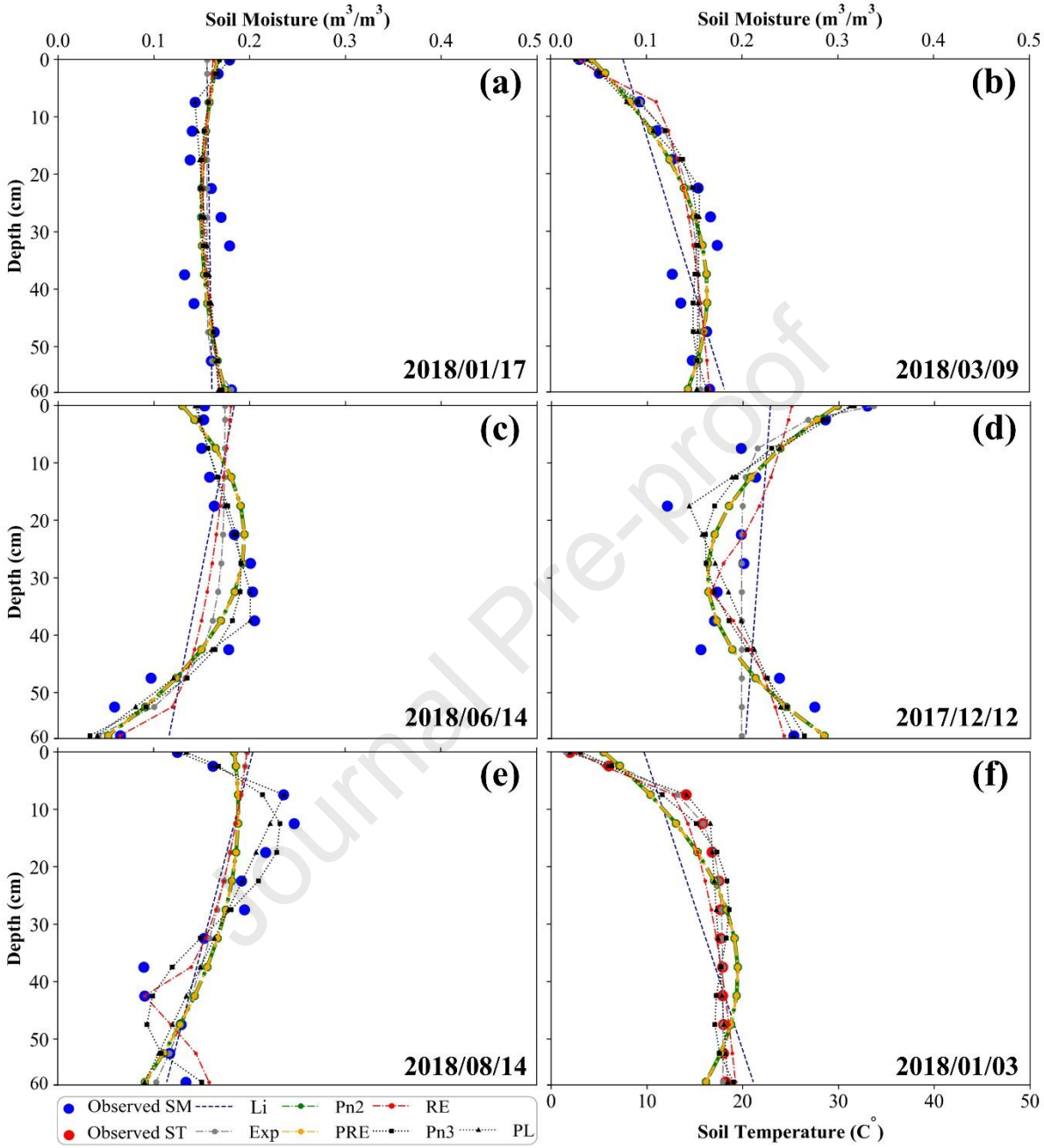

Fig. 4. Examples of (a) to (e) soil moisture and (f) soil temperature profile shapes encountered in Cora Lynn over the period December 2017 to December 2019 along with fitted mathematical functions (Li: Linear, Exp: Exponential, Pn2: second-order Polynomial, PRE: Parametrized second-order polynomial from simplified solution of Richard Equation, RE: simplified solution of Richards' Equation, Pn3: third order Polynomial, and PL: Piecewise Linear). Note: Both Pn2 and PRE functions resulted in exactly the same values, meaning that the curves were overlapped.

brings greater challenges to identify them. In this research, Eq.11 to Eq.16 and Eq.21 were considered as the mathematical representation of soil moisture profiles.

3.3 Inversion scheme

Radiative transfer equations used for forward models like the Njoku model need the distribution of soil moisture and temperature throughout the profile to simulate TB at the sensor level. Moreover, the output from the forward model should be able to closely mimic the TB that would be recorded by the sensor. Critically, validity of the forward model is a prerequisite for success of the inverse problem. For the synthesis study, it was assumed that the forward model met this criterion, while for the field application, roughness parameters were first calibrated to an independent period of data. In order to estimate the soil moisture profile, each of the above assumed mathematical functions was applied to calculate soil moisture as a function of depth. Accordingly, the parameters of the associated mathematical function were derived from matching predicted and observed TB using the cost function in Eq.22 through the coherent model in Eq.5 and Eq.6 by the process explained in Fig. 6. Accordingly, using the Njoku model the TB expected from an L-band and P-band radiometer were simulated separately and constrained using Eq.22.

$$L(\bar{X}) = \frac{1}{N}\left[\sum_{p=h,v}\left|TB_{f,p}(\bar{X}) - TB_{f,p}\right|^2\right], \tag{22}$$

where $(\bar{X})$ represents the parameters of interest, $TB_{f,p}$ and $TB_{f,p}(\bar{X})$ are the calculated and observed TB, N is the number of observations, p and f represent the polarization (H or V) and frequency, respectively.

Given the complex analytical form of this physics-based emission model, an iterative optimization scheme was used to minimize the cost function and estimate the desired soil moisture profile parameters of interest. Different optimization algorithms were analysed, including simulated annealing (SA), genetic algorithm (GA), particle swarm optimization

(PSO) and their combinations, to estimate soil moisture profiles under two nominal conditions (a dry case and a wet case). According to the results (not shown here), PSO alone consistently produced the best results and so was selected for optimization of the soil moisture profile shape parameters in this study. PSO is a stochastic evolutionary computation technique that relies on the social behavior of swarms of fish, bees, and other animals. Each solution in PSO can be considered as a particle, except that they share their information and interact locally with each other and with the community. These interactions lead to a global behavior which is less likely to get stuck in a local minimum. A schematic of the algorithm search for the global minima is shown in Fig. 5. By randomly initializing parameters, any particle (blue circle in Fig. 5 (a)) in the search space has an initial position whose value is the cost function. The next position of the particles is determined by Eq.23:

$$x^i[\,t+1] = x^i[\,t] + v^i[\,t+1] \tag{23}$$

$$v^i[\,t+1] = wv^i[\,t] + c_1 r_1\left(x^{i,best}[t] - x^i[t]\right) + c_2 r_2\left(x^{gbest}[t] - x^i[t]\right), \tag{24}$$

where $x^i[\,t]$ is the current position of the particle, $v^i[\,t+1]$ (Eq.24) is the speed for the next position which is a function of movement in the direction of the previous position $wv^i[\,t]$, the best experience of the particle $x^{i,best}[t] - x^i[t]$ and movement in the direction of the best

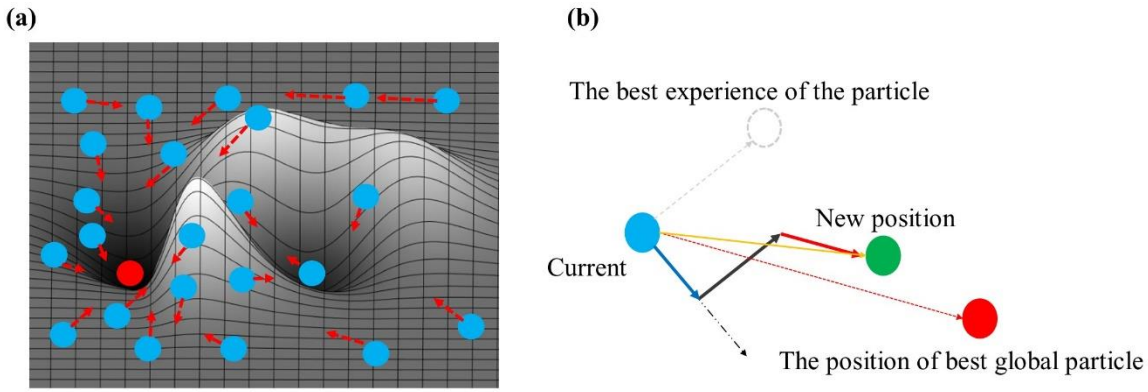

Fig. 5. (a) Schematic view of the particle swarm intelligence and (b) movement of a particle based on the theory of the PSO algorithm.

particle $x^{gbest}[t] - x^{i}[t]$, w is inertial weight between 0.6 and 0.9, slowing the particle and helping it to converge around x^{gbest}, c_1 and c_2 (between 1.2 and 1.5) are acceleration constants and r_1 and r_2 are random numbers between 0 and 1. A sample of the movement for one particle is shown in Fig. 5 (b).

Different strategies were considered to retrieve the soil moisture profile shape parameters (as shown in Fig. 6), including using the a) L-band observations alone, b) P-band observations alone, c) L- and P-band observations jointly (namely LP method), and d) retrieving the surface soil moisture parameter in each of the functions using the L-band observation and the rest of the shape parameters using the P-band observation (namely L_P method). In the L_P method, the soil moisture profile was first estimated using the L-band alone (method (a)). Because L-band is more sensitive to surface soil moisture, just the parameter related to the surface soil moisture in each of the used mathematical functions (parameter c in Eq.11 to Eq.15 and parameter θ_1 related to Eq.16 and Eq.21) was accepted and fed into the next step, which then retrieves the remaining parameters using P-band. It should be noted here that the estimated surface soil moisture using the coherent stratified model from L-band is the soil moisture at the air-soil interface and not the average soil moisture from surface to 5 cm depth. In order to compare the result of the different strategies, the number of iteration (100) and the parameters of the PSO algorithm (w, c_1 and c_2) along with the convergence criteria (< 0.01 K) for minimizing the cost function were considered equal. A flowchart of soil moisture profile estimation using the coherent stratified model is shown in Fig. 6.

In soil moisture profile estimation using each of the strategies, first a mathematical function was considered and then the corresponding parameters of the function were generated randomly and dependently. In applying all of the seven mathematical functions, first, surface soil moisture as a parameter of the function was generated and then the rest of the parameters were generated in a way that the change of soil moisture from the surface to the investigated

depth did not exceed 0.35 m^3/m^3 to prevent generating strange soil moisture profile shapes. The generated soil moisture profile along with the observed (or approximated) soil temperature profile was then fed into the Njoku model, and the TB at L-band and/or P-band simulated. In the LP method, the Njoku forward model is run twice in a sequential manner, once for the L-band and once for the P-band. The Njoku model is a multilayer model which is a function of the soil profile (taken to be to 1 m depth in our application), thereby negating the necessity for any assumptions regarding the different observation depths of L-band and P-band (Shen et al., 2020). The simulated TB was then compared with the observed TB collected from the radiometers mounted on the tower (or the synthetic equivalent) using the cost function in Eq.22. For estimating each soil moisture profile, the total 100 iterations and a population of 50 particles were considered. If the cost functions of ten successive iterations remain almost

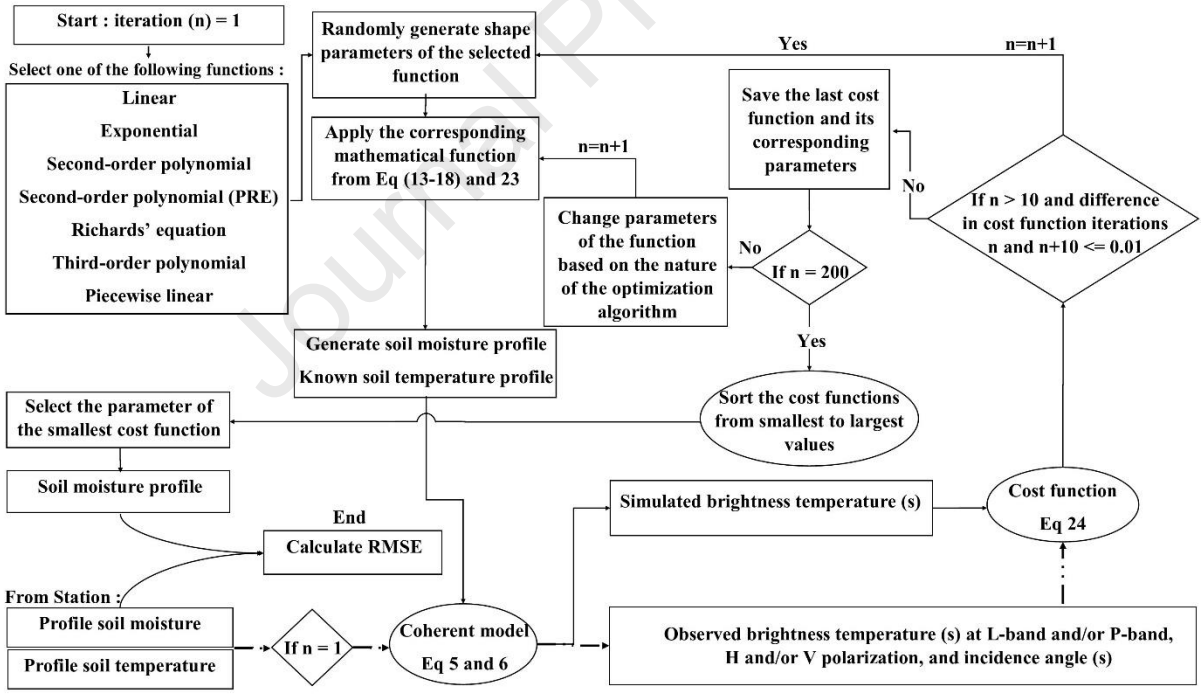

Fig. 6. Flowchart of soil moisture profile retrieval using the stratified coherent model. Note: here the soil moisture profile was retrieved using the L-band alone, P-band alone, and joint L- and P-band as explained in the text. For method L_P, first the soil moisture profile was retrieved based on this flowchart using L-band. In the next step, the soil moisture profile was retrieved using P-band alone but with the surface soil moisture parameter as already retrieved using L-band.

403 constant (< 0.01 K), then the algorithm interrupts the optimization process by changing the
404 parameters w, c_1 and c_2, and randomly generating a new population. The algorithm saves the
405 last cost function and the corresponding parameters in a separate matrix and starts generating
406 parameters from the beginning. If it doesn't get stock in the local minimum, it generates the
407 parameters so that it will converge the cost function. Finally, the matrix containing the smallest
408 cost function of each ten successive iteration were sorted based on its cost values and the
409 corresponding parameters of the smallest selected as the final output. The soil moisture profile
410 was then calculated from the retrieved parameters using the corresponding mathematical
411 function and the RMSE between estimated and observed soil moisture profile calculated.
412 Moreover, the practical depth for estimating the soil moisture profile from the relevant
413 mathematical function with a satisfactory level of accuracy (RMSE less than 0.04 m^3/m^3) was
414 approximated.

415 Experimental data of various soil moisture and temperature profile shapes (Fig. 2) collected
416 from ground Stations 126 and 136 in Cora Lynn under flat bare soil were used as input to the
417 coherent model to demonstrate the potential for profile estimation. Retrieved shape parameters
418 for the soil moisture profile were evaluated by comparing the derived profile against the
419 original profile used to produce the observed TB, with and without TB error imposed. A
420 uniform distribution of noise (low noise: -1 ~ +1 K, and high noise: -4 ~ +4 K) was imposed
421 on the TB observations, and each soil moisture profile estimated 10 times (realization) using
422 different realizations of noise. The analysis considered single and dual-frequency, single and
423 dual-polarization, and single and multi-incidence angle, snapshot and time series. Additionally,
424 the soil temperature profile was considered as known, or assessed for approximation using a
425 simple method.

426 In approximating the soil temperature profile, first a time series of the 6 AM profiles was
427 extracted from discrete measurements and interpolated to a continuous profile. The 12 soil

temperature measurements of each profile were related to depths of 2.5 (0-5 cm) to 57.5 (55-60 cm) in 5 cm increments. The gradient between 2.5 and 7.5 cm was used to estimate the soil temperature at the surface. The soil temperature below 57.5 cm up to 100 cm was considered constant and equal to the soil temperature at depth of 57.5 cm. Second, a general profile was calculated based on the whole set of 6 AM soil temperature profiles. Then surface soil temperature (measured or estimated from a land surface model) for that day could be added to the general profile shape and the soil temperature profile of that day approximated. The reason behind using the general profile shape lies in the fact that 6 AM soil temperature profiles through the year have a similar profile shape, but with an offset.

4. Results and discussion

In this section, the result from the soil moisture profile estimation methods as described in section 3.3 are first presented and discussed. The performance of the best method from the synthetic study is then evaluated using experimental data.

4.1 Soil moisture profile estimation

To explore the potential of the proposed soil moisture profile estimation models explained in the methodology section, the 20 soil moisture profiles shown in Fig. 3 were estimated individually using the four methods with dual H and V polarization, incidence angle of 40°, and the seven mathematical functions used to represent the soil moisture profile. The average final value of the cost function in the case of low (0.58 K) and high (0.96 K) noise scenarios using the LP method demonstrated the robustness of the inversion scheme. The depth for reliable estimation and error (RMSE) was calculated for each soil moisture profile at different depths over the top 60 cm profile, containing in situ soil moisture measurements at 12 depths. The result (Fig. 7 for high noise scenario and Fig-Sm. 1 in supplementary material for low noise scenario) showed that as the depth increased, the RMSE typically increased because of the reduced contribution of the soil dielectric profile to the total emission from the soil.

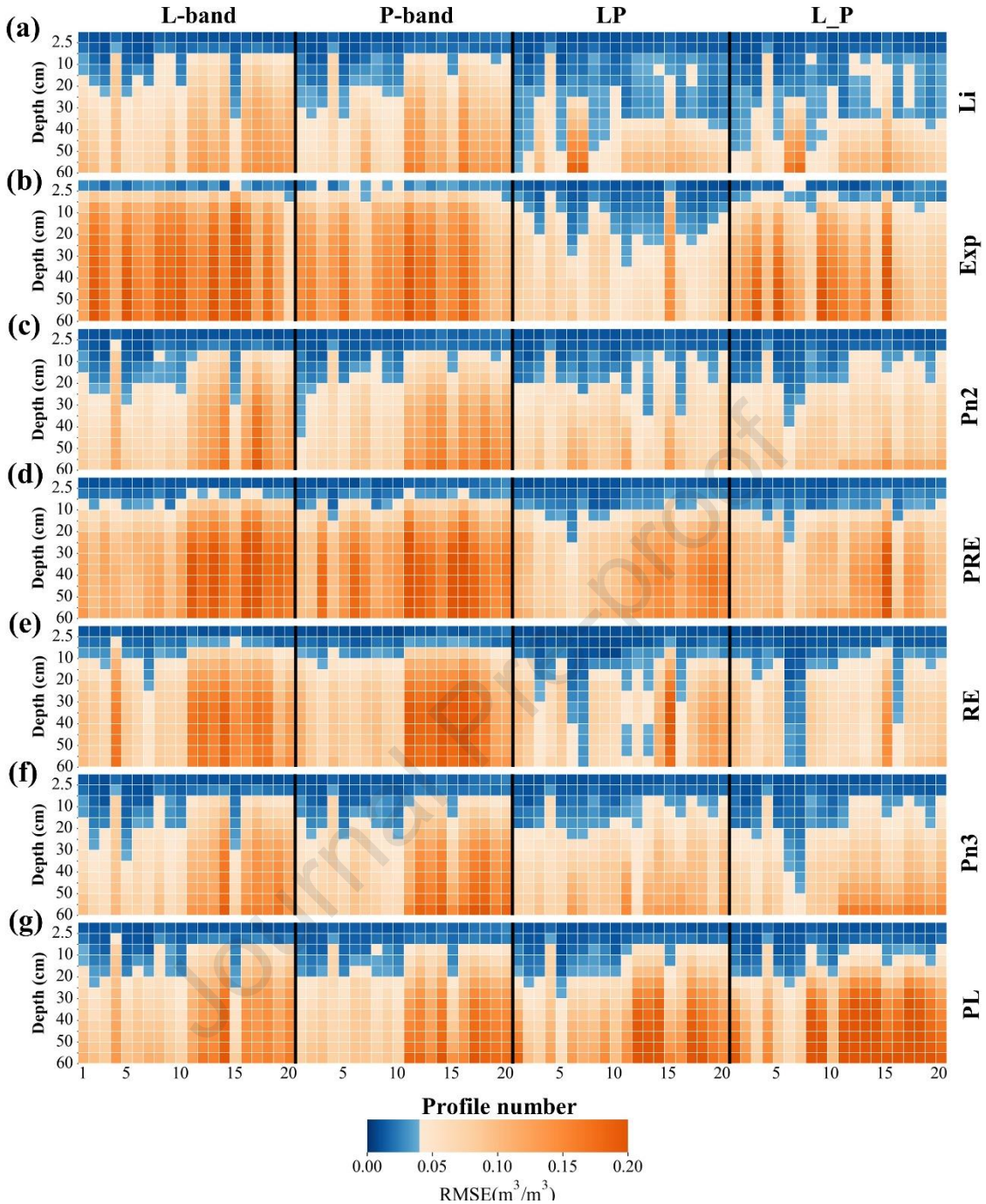

Fig. 7. Heatmap of RMSEs (average of ten perturbations under high noise scenario) between retrieved and observed soil moisture profile using L-band only (first column), P-band only (second column), LP band jointly (third column), and L_P method (last column). Each row shows results for a mathematical function representing the soil moisture profile including (a) linear, (b) exponential, (c) second-order polynomial, (d) derived second order polynomial from simplified solution of Richard equation, (e) simplified solution of Richard equation, (f) third-order polynomial, and (g) piecewise linear. Note: the blue color represents the RMSE below the target RMSE (0.04 m3/m3).

453 Moreover, it was found that the RMSE of the methods was lower for Period A (profile numbers

1 to 10 in Fig. 7 and Fig-Sm. 1) as compared to Period B (profile numbers 11 to 20 in Fig. 7 and Fig-Sm. 1) due to the higher penetration depth of L- and P-band wavelengths in drier profiles (Rao et al., 1988). Taking all the mathematical functions and the twenty soil moisture profiles into account, it was found that the LP method outperformed other methods (Fig. 8). The two different levels of noise in the synthetic study aimed to represent the impact of calibration and model uncertainty. The average estimation depth of the methods under low (high) noise scenarios were 5 (4) cm at L-band, 6 (5) cm at P-band, 13 (12) cm with LP method, and 11 (10) cm for L_P method. Thus, it is clear that the performance of the two wavelengths together is better than the performance of a single wavelength. Since the sensitivity to factors which affect soil emission is frequency dependent (e.g. penetration depth is increased in the soil at longer wavelengths), obtaining higher accuracy and getting information from deeper layers are expected to be achieved by combining the two L-band and P-band frequencies. More specifically, there are many profile options that could lead to the same P-band TB prediction. However, adding an additional frequency at L-band constrains these options and thus leads to

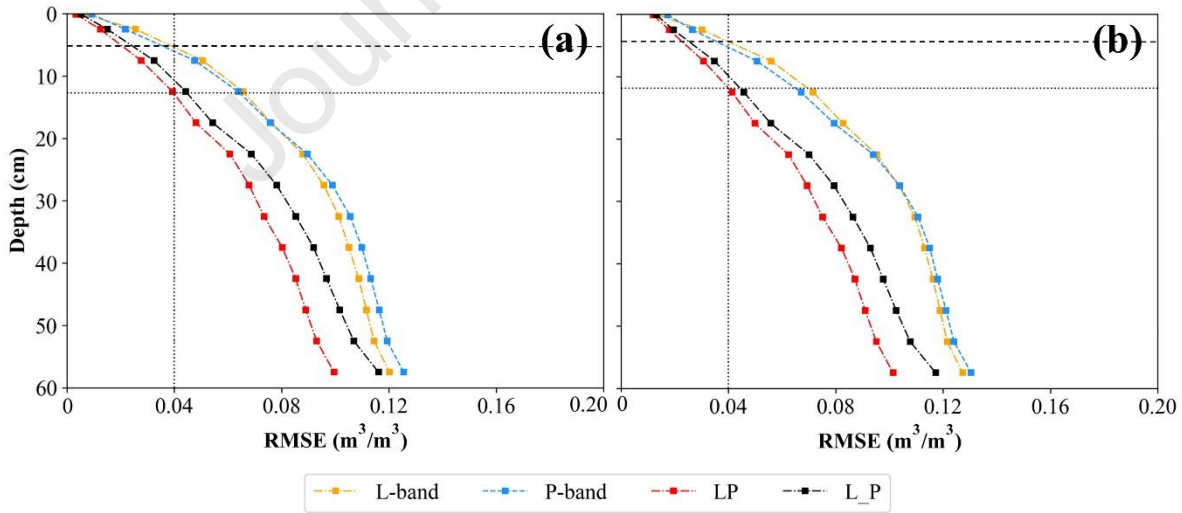

Fig. 8. Comparison of the methods for (a) low noise and (b) high noise scenario. Note: the RMSE axis is the average RMSE of 10 realizations and 7 mathematical functions. The vertical and horizontal dotted lines show the target RMSE (0.04 m3/m3) and the associated maximum estimation depth respectively. The dashed horizontal line shows worst case scenarios of estimation depth.

a more accurate extrapolation. The L_P method was the next best performing method followed by the P-band and finally L-band only models. Regardless of the applied noise scenario or the period, the RMSE of the L-band model predicted shallower surface soil moisture than the P-band model (Fig. 8). This is because the P-band signal carries information about the soil moisture from much deeper layers of the soil. The performance of the individual mathematical functions representing the soil moisture profile was investigated. For this reason, the estimation depth of the methods was calculated as shown in Fig. 9. The linear function with only two parameters (Eq.11) could estimate the soil moisture up to a depth of 31 cm (mean of low and high noise scenarios) at LP and 30 cm at L_P method, outperforming all other functions. Additionally, the average estimation depth of the Pn2 function (17 cm) was comparable with Pn3 (17.5 cm) using each of the LP or L_P methods. The RE function recommended by Sadeghi et al. (2016) led to an estimation depth of 12 cm at both LP and L_P methods. The PL function using LP (L_P) method was the next best function with estimation depth 9 (12) cm. Although applying the Exp function resulted in an estimation depth of 12 cm using the LP method, the lowest estimation depth was achieved using this function with 1 cm at L-band alone, 2 cm at P-band alone and 4 cm for L_P method. Also, using the PRE function an average estimation depth of 4 cm (10 cm) was achieved using L-band or P-band (LP or L_P) methods. The reason

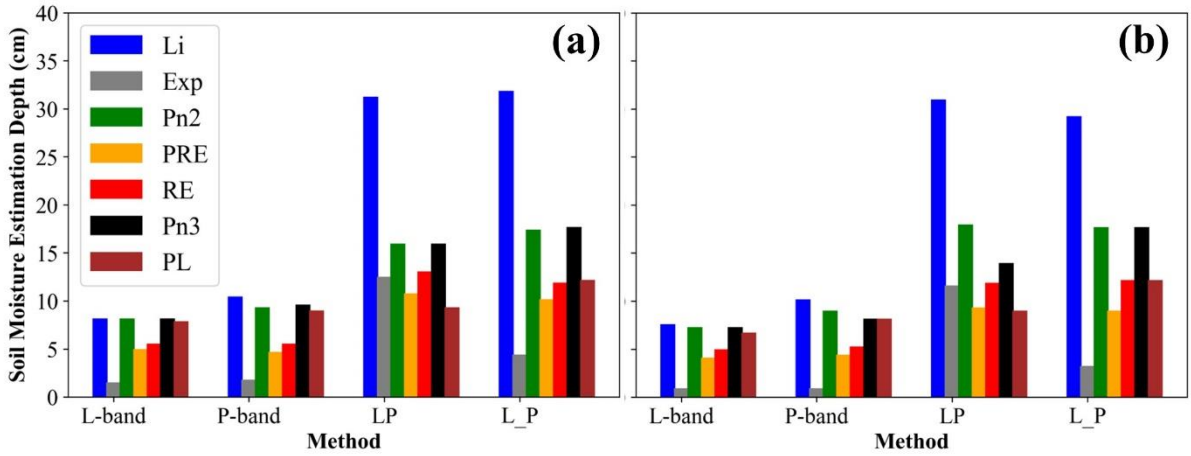

Fig. 9. The estimation depth of methods according to assumed moisture profile functions based on target RMSE 0.04 m3/m3 under (a) low and (b) high noise scenarios.

485 of achieving lower estimation depth using the Exp function could be linked to the fact that a
486 small change in the shape parameters (a and b in Eq.12) of this function leads to a huge change
487 in the profile shape. Additionally, function PRE could capture the shape of the profiles that are
488 dominant in Period B (Fig. 3). Except Exp, PRE, and RE functions, the depth of estimation of
489 the other functions were similar using L-band or P-band methods and were 8 cm and 9 cm
490 respectively. The results obtained using the employed functions were similar at least for depths
491 less than 10 cm (Fig. 7 and Fig. 10). Therefore, if the intention is to estimate the soil moisture
492 not deeper than 10 cm, any of these functions can be expected to give a similar result. The
493 linearity of soil moisture variation at the lower depth could be a possible reason for achieving
494 such similar results, thus enabling most of these functions to capture the shape of the profile at
495 the lower depths. However, as the depth increased, the RMSE between the estimated and
496 observed soil moisture profile increased (Fig. 7 and Fig. 10). This synthetic study clearly shows
497 the effectiveness of the LP method in estimating the soil moisture profile with the best
498 mathematical functions of Li followed by Pn2 function. Therefore, the LP method was selected
499 as the most robust method and thus the main focus of the further analysis of this research.

500 *4.2 Time series estimation of soil moisture profile*

501 The optimization algorithm (PSO) used in this study is population-based and so the particles
502 share information together while searching the global minimum. In the snapshot retrieval, one
503 global minimum is found by 50 particles during every iteration. For example, considering a
504 second-order polynomial for retrieving parameters a, b, and c, the 50 particles search for
505 finding one global minimum. By increasing the number of observations (known) in a fixed
506 time-window, more parameters can be retrieved. If a 30 day estimation period of soil moisture
507 profiles is considered using the second-order polynomial function instead of retrieving one set
508 of a, b, and c, 30 sets of parameters are retrieved. However, in a drying down period, these 30
509 parameters of a, b, and c change gradually and so can build a density of global minima in the

search space. As a result, finding 30 global minima (built by 30 days × 3 parameters) by 50 particles is much easier than finding one global minimum. Accordingly, PSO is expected to give a better result with the time series approach, because it is able to incorporate the prior knowledge of the previous time step to get the value for the next time step as it understands the relationship between these parameters through time. As a result, the motivation of using time series retrieval is proposed.

The temporal behaviour of soil moisture is usually characterized by a relatively slow dry-down process following an abrupt increase from precipitation or irrigation. Therefore, dry down periods of soil moisture in Period A and B were considered to compare the time series and snapshot retrieval methods. The purpose of selecting the dry-down periods was for partially removing the uncertainties in calibration and forward modeling in the multi-temporal soil moisture profile estimation. The Period A is characterized by simple soil profile shapes and relatively lower soil moisture with average 0.13 m^3/m^3 (minimum 0.07 m^3/m^3 and maximum 0.23 m^3/m^3) while Period B has more complex profile shapes with an average of 0.27 m^3/m^3 (minimum 0.13 m^3/m^3 and maximum 0.35 m^3/m^3). Fig. 10 shows the comparison between the snapshot and time series estimation for the two periods using the LP method. It is concluded that except the Li function, the time series outperformed the snapshot estimation under low (high) noise scenario by 0.01 (0.01) m^3/m^3 for RE, 0.01 (0.02) m^3/m^3 for PRE, 0.02 (0.02) m^3/m^3 for PL, 0.008 (0.01) m^3/m^3 for Exp, 0.004 (0.008) m^3/m^3 for Pn3, and 0.006 (0.002) m^3/m^3 for Pn2 functions. Function Li showed an exception in which RMSE increased by 0.006 (0.003) under low (high) noise scenarios when using the time series approach.

The effect of combining observations from different incidence angles, including 10, 20, and 40°, on the soil moisture profile estimation accuracy as compared to having observations at a single incidence was assessed using the L-band, the P-band, and the LP method. It was found that using one incidence angle at 40° with the LP method outperformed using multi-incidence

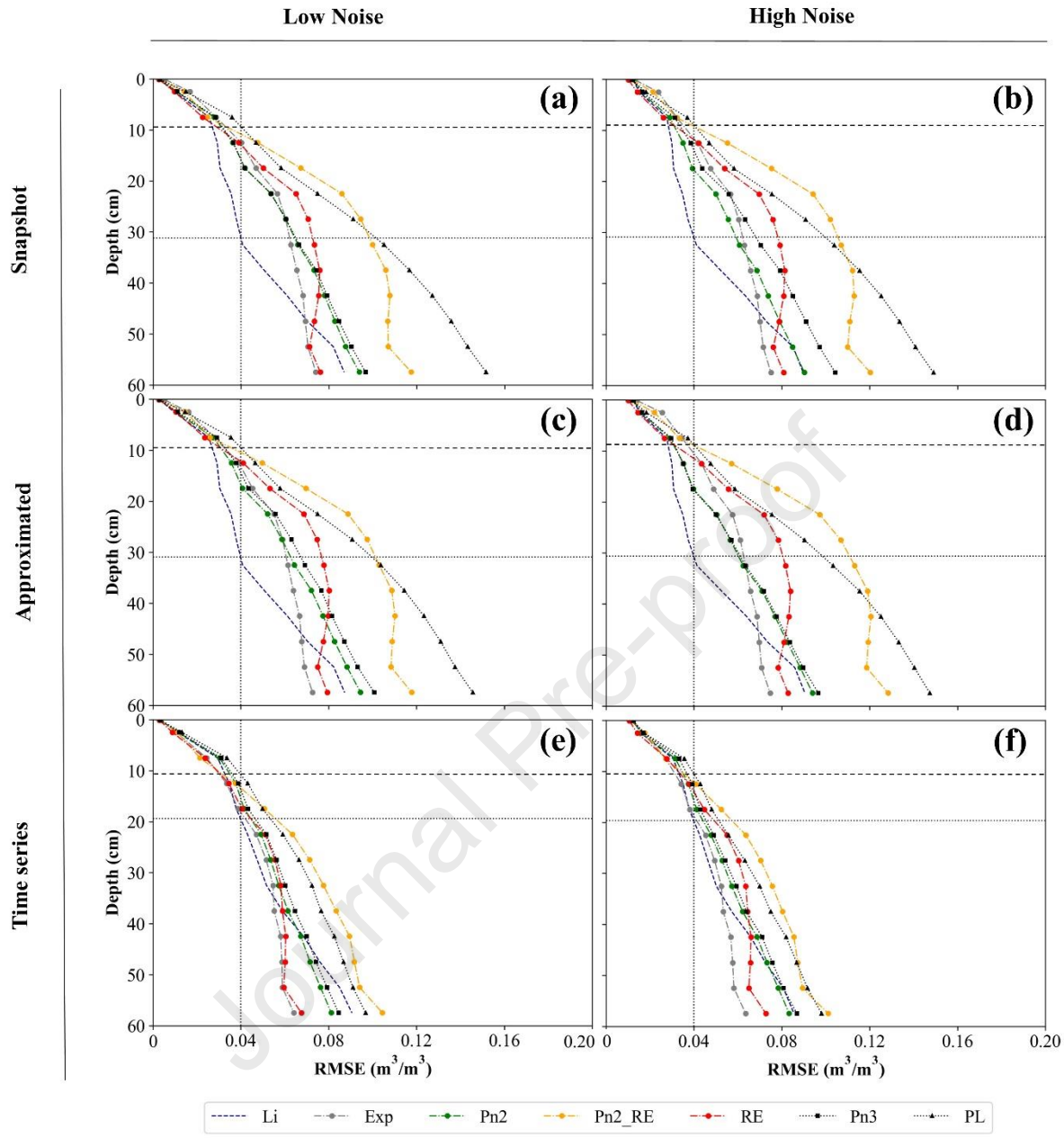

Fig. 10. Snapshot retrieval of soil moisture profiles using the combined L- and P-band method (H and V polarization and single 40° incidence angle) for (a and b) known and (c and d) approximated soil temperature profile using snapshot retrieval, and time series retrieval (e and f) with known soil temperature profile under low and high noise scenarios. The dashed and dotted horizontal lines show best and worst case scenarios of estimation depth.

angles at L-band or P-band alone (Fig-SM. 2). Taking all the mathematical functions into account, the result of the LP method using a combination of different incidence angles, including 40°, 20 and 40°, and 10, 20 and 40° demonstrated (Fig-SM. 3) that two incidence

angles resulted in a 0.003 m^3/m^3 decrease in RMSE under low and high noise scenarios, while remaining unchanged when three incidence angles were employed.

Investigation of single and dual-polarization retrieval from the LP method confirmed expectations (Fig-SM. 4) that using H and V together resulted in better performance than when using either polarization individually.

4.3 Impact of approximation of soil temperature profile on the estimation accuracy

The soil temperature profile is one of the important inputs of the microwave coherent model in simulating TB, but obtaining this variable is challenging and has thus been a limitation for large-scale applications. Therefore, an approximation method as explained in the methodology section was considered and differences quantified between the approximated profiles from actual temperature profiles and their impact on the simulated TB and soil moisture estimation. It was found (not shown here) that approximation of the soil temperature profile leads to an average RMSE between actual soil temperature profiles at 6 AM and approximated soil temperature of around 3 K.

The impact of the soil temperature profile approximation on the TB estimation for soil moisture profile estimation was investigated. Accordingly, TB was simulated for both L-band and P-band using the coherent model from actual and approximated soil temperature profiles. Considering the thermal sensing depth at L-band and P-band, it is obvious that if approximated soil temperature profiles were calculated from the surface soil temperature, the RMSE of the simulated and observed TB would be higher at P-band (4 K) as compared with L-band (3 K). The reason is that thermal sensing depth at P-band is much deeper than for L-band, and P-band is more sensitive to the temperature of the deeper layers. In the above analysis, a dry soil moisture profile was considered. However, when a wet soil moisture profile was considered, a much lower RMSE of TB was achieved when using the approximated soil temperature profile. The reason is that when soil moisture is high, the penetration depth and the variation of soil

temperature near the surface decrease so that surface temperature is more realistic for approximating the soil temperature profile.

It should be noted that, to investigate the impact of approximated soil temperature profiles on soil moisture profile estimation, the twenty soil moisture profiles (Fig. 3) were estimated individually using the LP method under low and high noise scenarios (Fig. 10 (c and d)). In the low noise scenario, except Exp (decrease in RMSE by 0.001 m^3/m^3), Pn2 (decrease in RMSE by 0.0005 m^3/m^3), and PL (decrease in RMSE by 0.001 m^3/m^3) function, and in the high noise scenario except Pn3 (decrease in RMSE by 0.005 m^3/m^3) and PL (decrease in RMSE by 0.0001 m^3/m^3) functions, the retrievals from other functions were a little worse by average 0.002 m^3/m^3. Therefore, the approximation method of soil temperature profile can be considered as an appropriate substitution of having known soil moisture profile information when estimating the soil moisture profile using coherent models.

4.4 Estimating soil moisture profile using real experiment data

In the synthetic study it was found that the LP method outperformed other methods, and that using the time series approach gave better performance compared with snapshot retrieval. Additionally, it was concluded that the two incidence angles 10° and 40° at both H and V polarization led to the lowest RMSE. It was also shown that Li and Pn2 functions resulted in a lower RMSE compared with the other options. Thus, using this configuration, the coincident brightness temperature observations at L-band and P-band for the Period A and B profiles shown in Fig. 2 were used for testing with real data. In the real study using real data, because of the configuration of the tower, the brightness temperature observations were only available at incidence angles of 45° (for Period A) and 40° (for Period B) for both L-band and P-band. Therefore, the soil moisture was estimated using a single incidence angle. To assess the performance of the proposed inversion scheme, the L-band and P-band observations (Fig. 2 (c); 26 days in Period A and 14 days in Period B) were first used along with simultaneous

588 measurements of soil moisture and temperature profiles (Fig. 2 (a and b)) for the two periods
589 from the PRISM project. The numerical setup of the coherent model was considered the same
590 as for the synthetic study with the same profile depth and number of layers. The brightness
591 temperature was simulated using the coherent forward model and evaluated against
592 observations at L-band and P-band for both periods. As explained in the methodology section,
593 the roughness parameters h_P, q_P, and n_P in Eq.7, and soil temperature profile were considered
594 as known.

595 Fig. 11 shows the predicted brightness temperature versus the respective L-band and P-band
596 observations over the two Periods A and B. The V (4.4 K) and H (4.6 K) polarization achieved
597 the best performance for L-band and P-band respectively, followed by V (6.9 K) and H (8.6 K)
598 polarization at the P-band and L-band. The H polarization is more sensitive to roughness and
599 so this could be the possible reason for higher RMSE at L-band compared with the V
600 polarization. Following rainfall when the surface was drying out, the anomalous error in H
601 polarization at L-band led to higher observed TB. However, the model used the average soil

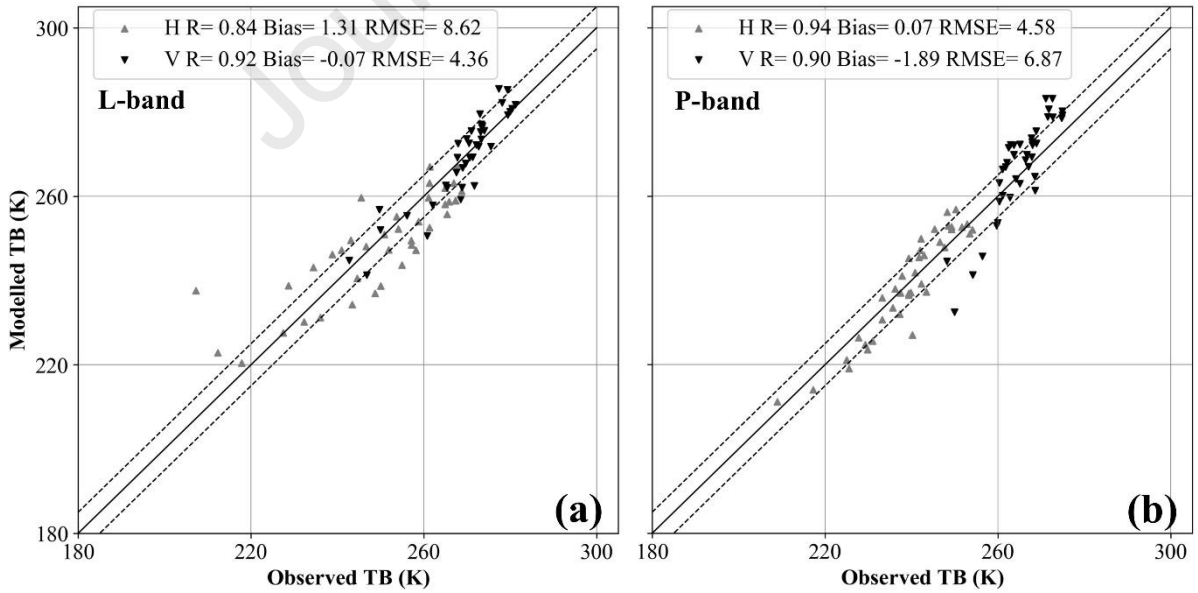

Fig. 11. Comparison of calculated brightness temperature from the coherent model and tower observations at (a) L-band and (b) P-band over bare soil. The dash lines denote ± 5 K offset. R refers to the Pearson correlation coefficient.

moisture below the surface (measured by ground stations), which was wetter than the surface (due to infiltration), resulting in a relatively lower modelled TB. The source of anomalous error in P-band and V polarization is unknown, with the model overestimating the TB. None of these errors were removed from the calculations. Notably, there is a tendency for the Njoku model to underestimate (overestimate) at low (high) soil moisture (especially at L-band) (Njoku and O'Neill, 1982). Reasons for differences include: i) during a dry period, the soil moisture at the skin is lower and drier than the deeper profile while during the wet period (especially during rainfall), the surface tends to be saturated and it is wetter than deeper profiles; ii) wind and rain showers modify the surface and the differences between surface roughness characteristics change; iii) the skin soil moisture was constructed by having the slope of soil moisture variation estimated using the sensor values at 2.5 and 7.5 cm which might not be realistic.

In the synthetic study, it was found that applying the LP method using a linear and a second-order polynomial within a time series retrieval resulted in the lowest RMSE. As a comparison to the synthetic study, the soil moisture profiles were estimated for Periods A (26 days) and B (14 days) using the LP model using the seven mathematical functions with both the time series and snapshot approaches. The result in Fig. 12 shows that using snapshot (time series approaches) the soil moisture profiles were estimated with lower RMSE in Period A (average 11 cm (21cm) estimation depth) as compared with Period B (average 4 cm (5cm) estimation depth). The reason is that during the dry period when all layers had low moisture, the L-band and P-band had a deeper observation depth. During the dry period (Period A), the time series approaches outperformed the snapshot retrieval with an increasing estimation depth of 20 cm for Exp, 15 cm for PL, 10 cm for Pn2 and Pn3, 5 cm for PRE and RE, and 3 cm for Li, resulting in average increase of 10 cm. During the wet period (Period B), the time series approach still resulted in an average increase of 1 cm, with 4cm, 4cm, and 3cm increase in estimation depth

of Exp, RE, and PRE respectively, unchanging for Pn3 and PL, and 1 cm decrease for Pn2 and Li functions. The time series approach using the LP method was found to be the most robust with a minimum estimation depth of 8 cm using the PRE function and maximum estimation

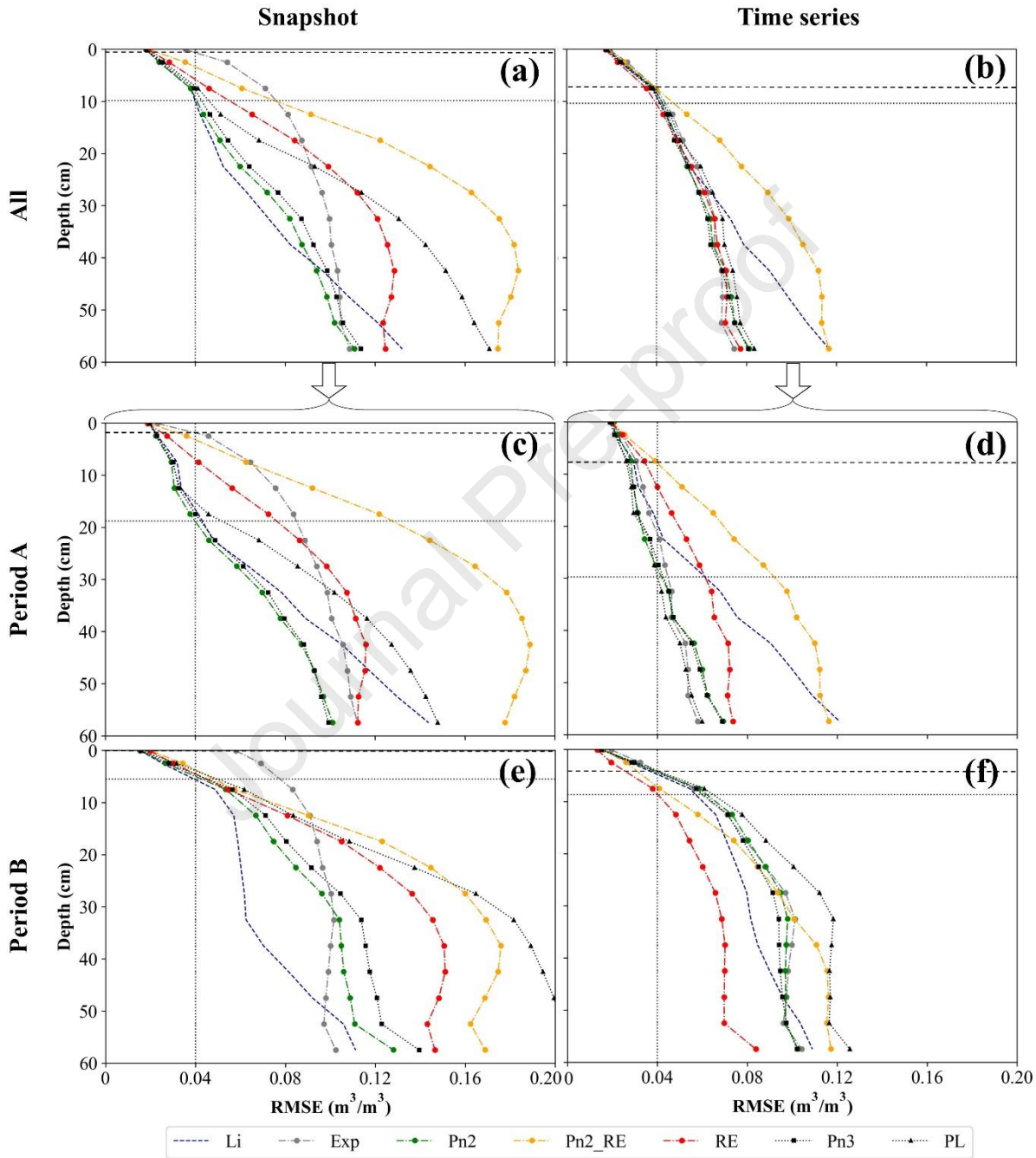

Fig. 12. The average RMSE calculated between in-situ and retrieved soil moisture profiles using LP method for (a) snapshot and (b) time series approaches decomposed to Period A (c and d) and Period B (e and f). The dashed and dotted horizontal lines show best and worst case scenarios of estimation depth.

depth of 28 cm using Pn2 and Pn3 functions over period A. Additionally, the result of the time series approach for Period B had the minimum estimation depth of 5 cm using L, Exp, Pn2, Pn3, and PL, and maximum estimation depth of 8 cm using the PRE and RE functions. Besides, the time series approach is faster (0.5 second faster in retrieving each profile) and more precise (standard deviation 0.015 (0.016) m^3/m^3 at the surface; 0.05 (0.06) m^3/m^3 at depth of 60 cm for time series (snapshot) with lowest values for the Pn2 function) than the snapshot retrieval approach. Moreover, the Exp, PRE and PL functions were found to be more sensitive to noise in the observed brightness temperature compared to the other functions, resulting in the snapshot retrieval approach having a higher RMSE when using these functions. In contrast, the RE function is not sensitive to noise, however under some conditions (as explained in the methodology) it has to be replaced with the PRE function resulting in a higher RMSE. The time series retrieval can mitigate noise as explained in section 4.2 and so resulted in a much lower RMSE as compared with the snapshot retrieval.

From this analysis it is concluded that the Pn2 function is the best function for estimating soil moisture. Additionally, if the intention is estimating soil moisture below 20 cm, the Li function with only two parameters can be considered as the best representation of soil moisture profile especially during a wet season (Period B). The reason for a lower RMSE in the linear function is the linearity of soil moisture in the shallow layer so that it is captured by this function. The better performance of the PRE function during Period B is because during this period soil moisture profiles had a large gradient at the shallow layers (up to 20 cm) and also showed some changes of soil moisture value in the deeper layers, meaning that this function can capture their shapes more easily. Some samples of estimated and observed soil moisture profiles for both periods are shown in Fig. 13.

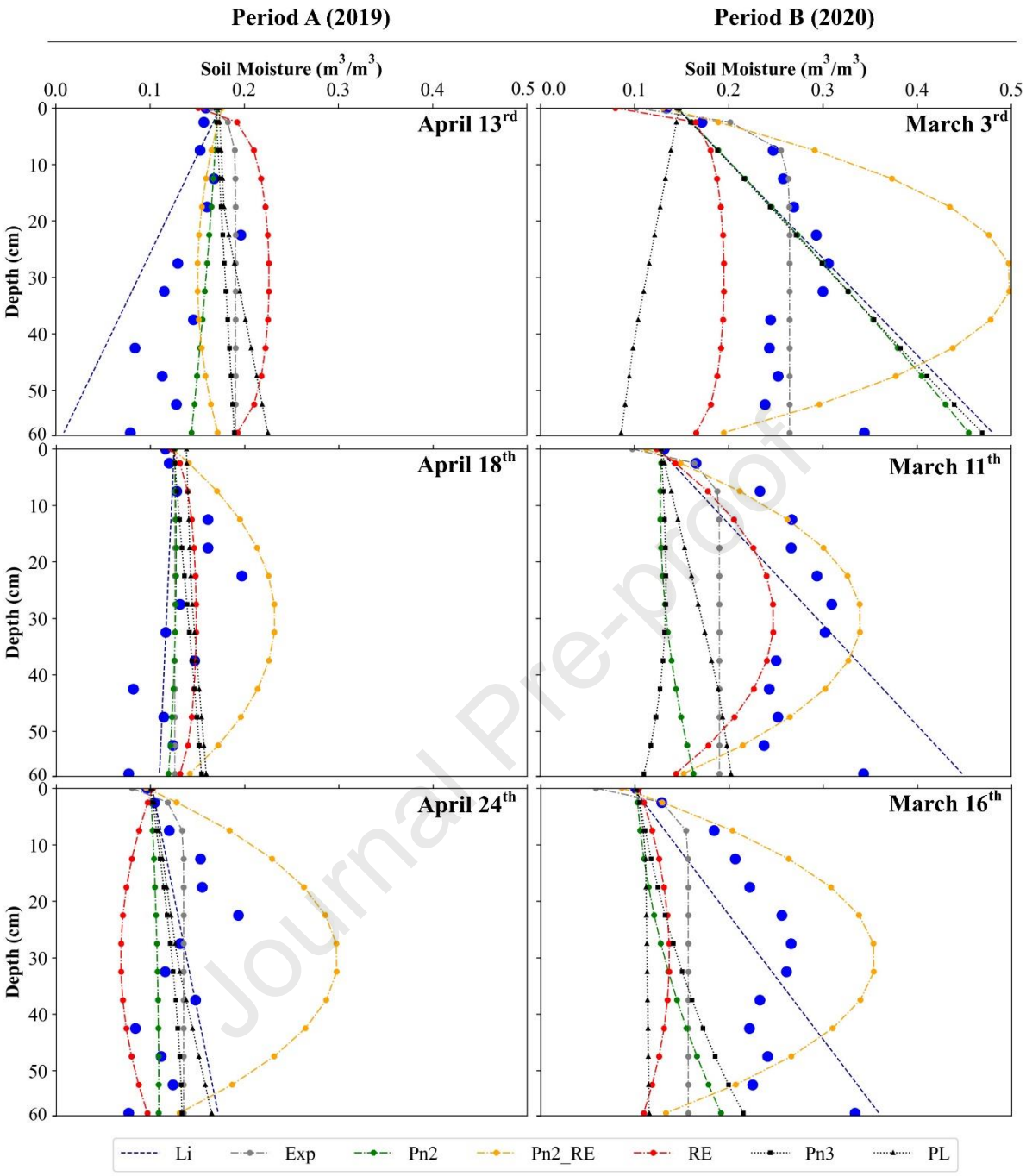

Fig. 13. Samples of estimated soil moisture profile using the LP method for the two periods A (left column) and B (right column) periods utilizing the time series approaches.

5. Conclusions

A soil moisture profile estimation strategy has been developed using L- and P-band radiometer observations together with a stratified coherent model and the PSO optimization algorithm.

Under low and high noise synthetic scenarios with RMSE lower than 0.04 m^3/m^3, the combined use of L- and P-band dual polarization data outperformed both the L- or P-band method alone, with an average estimation depth of 20 cm for the Li function and 15 cm for the Pn2 function under both a wet and dry period with complex profiles, providing the more robust time series approach was employed. Multi-incidence angle retrieval using 10° and 40° improved the average RMSE by 0.002 m^3/m^3 and 0.005 m^3/m^3 under low and high noise scenarios respectively as compared with single angle retrieval at 40°, while adding a third incidence angle of 20° made no further improvement. Moreover, when approximating the soil temperature profile with a simple method that uses a trend of the profile together with a surface soil temperature measurement, there is little impact on the result. In a real-world experiment, the combined L-band and P-band method using the time series retrieval approach and a second-order polynomial representing the soil moisture profile outperformed the other methods tested, with an RMSE less than 0.04 m^3/m^3 for depths up to 28 cm for a dry period but only to 5 cm for a wet period. The success of this work demonstrates the potential of this approach, which now requires further research to determine the most suitable mathematical functions for soil moisture profile estimation in different regions around the world. Additionally, this study demonstrates the potential of combining L-band and P-band radiometry for estimating soil moisture in the root zone, proving the merit of this concept for the next generation radiometer satellite mission.

Acknowledgments

This work was supported by the Australian Research Council through the Towards P-Band Soil Moisture Sensing from Space Project under Discovery Grant DP170102373, and Linkage, Infrastructure, Equipment and Facility Grants LE0453434 and LE150100047. The authors wish to thank Pascal Mater and Kiri Mason for their help with the maintenance of the experimental equipment and site.

References

Azemati, A., Etminan, A., Tabatabaeenejad, A., Moghaddam, M., 2019. Retrieval of Subsurface Soil Moisture Profiles from L-Band and P-Band Reflectometry, in: 2019 International Conference on Electromagnetics in Advanced Applications (ICEAA). Presented at the 2019 International Conference on Electromagnetics in Advanced Applications (ICEAA), IEEE, Granada, Spain, pp. 1328–1328. https://doi.org/10.1109/ICEAA.2019.8879216

Baldwin, D., Manfreda, S., Keller, K., Smithwick, E.A.H., 2017. Predicting root zone soil moisture with soil properties and satellite near-surface moisture data across the conterminous United States. Journal of Hydrology 546, 393–404. https://doi.org/10.1016/j.jhydrol.2017.01.020

Brocca, L., Moramarco, T., Melone, F., Wagner, W., Hasenauer, S., Hahn, S., 2012. Assimilation of Surface- and Root-Zone ASCAT Soil Moisture Products Into Rainfall–Runoff Modeling. IEEE Trans. Geosci. Remote Sensing 50, 2542–2555. https://doi.org/10.1109/TGRS.2011.2177468

Carranza, C., Nolet, C., Pezij, M., van der Ploeg, M., 2021. Root zone soil moisture estimation with Random Forest. Journal of Hydrology 593, 125840. https://doi.org/10.1016/j.jhydrol.2020.125840

Chen, R.H., Tabatabaeenejad, A., Moghaddam, M., 2018. P-Band Radar Retrieval of Permafrost Active Layer Properties: Time-Series Approach and Validation with In-Situ Observations, in: IGARSS 2018 - 2018 IEEE International Geoscience and Remote Sensing Symposium. Presented at the IGARSS 2018 - 2018 IEEE International Geoscience and Remote Sensing Symposium, IEEE, Valencia, pp. 6777–6779. https://doi.org/10.1109/IGARSS.2018.8518179

Chen, R.H., Tabatabaeenejad, A., Moghaddam, M., 2017. Retrieval of permafrost active layer properties using P-band airmoss and L-band UAVSAR data, in: 2017 IEEE International Geoscience and Remote Sensing Symposium (IGARSS). Presented at the 2017 IEEE International Geoscience and Remote Sensing Symposium (IGARSS), IEEE, Fort Worth, TX, pp. 1415–1418. https://doi.org/10.1109/IGARSS.2017.8127230

Chen, R.H., Tabatabaeenejad, A., Moghaddam, M., 2016. A time-series active layer thickness retrieval algorithm using P- and L-band SAR observations, in: 2016 IEEE International Geoscience and Remote Sensing Symposium (IGARSS). Presented at the IGARSS 2016 - 2016 IEEE International Geoscience and Remote Sensing Symposium, IEEE, Beijing, China, pp. 3672–3675. https://doi.org/10.1109/IGARSS.2016.7729951

Chu, X., Han, G., Xing, Q., Xia, J., Sun, B., Li, X., Yu, J., Li, D., Song, W., 2019. Changes in plant biomass induced by soil moisture variability drive interannual variation in the net ecosystem CO2 exchange over a reclaimed coastal wetland. Agricultural and Forest Meteorology 264, 138–148. https://doi.org/10.1016/j.agrformet.2018.09.013

Clark, M.P., Rupp, D.E., Woods, R.A., Zheng, X., Ibbitt, R.P., Slater, A.G., Schmidt, J., Uddstrom, M.J., 2008. Hydrological data assimilation with the ensemble Kalman filter: Use of streamflow observations to update states in a distributed hydrological model. Advances in Water Resources 31, 1309–1324. https://doi.org/10.1016/j.advwatres.2008.06.005

Cuenca, R.H., Hagimoto, Y., Ring, T.M., Beamer, J.P., 2016. Interpretation of In Situ Observations in Support of P-Band Radar Retrievals. IEEE J. Sel. Top. Appl. Earth Observations Remote Sensing 9, 3122–3130. https://doi.org/10.1109/JSTARS.2016.2582737

Das, N., Mohanty, B.P., 2006. Root zone soil moisture assessment using remote sensing and vadose zone modeling. Vadose Zone Journal 5, 296–307.

Du, J., Kimball, J., Moghaddam, M., 2015. Theoretical Modeling and Analysis of L- and P-band Radar Backscatter Sensitivity to Soil Active Layer Dielectric Variations. Remote Sensing 7, 9450–9472. https://doi.org/10.3390/rs70709450

Engman, E.T., Chauhan, N., 1995. Status of microwave soil moisture measurements with remote sensing. Remote Sensing of Environment 51, 189–198. https://doi.org/10.1016/0034-4257(94)00074-W

Entekhabi, D., Yueh, S., De Lannoy, G., 2014. SMAP handbook.

Etminan, A., Tabatabaeenejad, A., Moghaddam, M., 2020. Retrieving Root-Zone Soil Moisture Profile From P-Band Radar via Hybrid Global and Local Optimization. IEEE Trans. Geosci. Remote Sensing 1–9. https://doi.org/10.1109/TGRS.2020.2965569

Falloon, P., Jones, C.D., Ades, M., Paul, K., 2011. Direct soil moisture controls of future global soil carbon changes: An important source of uncertainty: SOIL MOISTURE AND SOIL CARBON. Global Biogeochem. Cycles 25, n/a-n/a. https://doi.org/10.1029/2010GB003938

Ford, T.W., Harris, E., Quiring, S.M., 2014. Estimating root zone soil moisture using near-surface observations from SMOS. Hydrol. Earth Syst. Sci. 18, 139–154. https://doi.org/10.5194/hess-18-139-2014

Gao, X., Zhao, X., Brocca, L., Pan, D., Wu, P., 2019. Testing of observation operators designed to estimate profile soil moisture from surface measurements. Hydrological Processes 33, 575–584. https://doi.org/10.1002/hyp.13344

Hu, W., Si, B.C., 2014. Can soil water measurements at a certain depth be used to estimate mean soil water content of a soil profile at a point or at a hillslope scale? Journal of Hydrology 516, 67–75. https://doi.org/10.1016/j.jhydrol.2014.01.053

Jiang, G., Wang, N., Zhang, Yaoyu, Wang, Z., Zhang, Yuling, Yu, J., Zhang, Yong, Wei, Z., Xu, Y., Geisen, S., Friman, V.-P., Shen, Q., 2021. The relative importance of soil moisture in predicting bacterial wilt disease occurrence. Soil Ecol. Lett. 3, 356–366. https://doi.org/10.1007/s42832-021-0086-2

Karthikeyan, L., Mishra, A.K., 2021. Multi-layer high-resolution soil moisture estimation using machine learning over the United States. Remote Sensing of Environment 266, 112706. https://doi.org/10.1016/j.rse.2021.112706

Karthikeyan, L., Pan, M., Wanders, N., Kumar, D.N., Wood, E.F., 2017. Four decades of microwave satellite soil moisture observations: Part 1. A review of retrieval algorithms. Advances in Water Resources 109, 106–120. https://doi.org/10.1016/j.advwatres.2017.09.006

Kerr, Y.H., Waldteufel, P., Wigneron, J.-P., Delwart, S., Cabot, F., Boutin, J., Escorihuela, M.-J., Font, J., Reul, N., Gruhier, C., Juglea, S.E., Drinkwater, M.R., Hahne, A., Martín-Neira, M., Mecklenburg, S., 2010. The SMOS Mission: New Tool for Monitoring Key Elements ofthe Global Water Cycle. Proc. IEEE 98, 666–687. https://doi.org/10.1109/JPROC.2010.2043032

Liang, X., Liakos, V., Wendroth, O., Vellidis, G., 2016. Scheduling irrigation using an approach based on the van Genuchten model. Agricultural Water Management 176, 170–179.

Mahmood, R., Littell, A., Hubbard, K.G., You, J., 2012. Observed data-based assessment of relationships among soil moisture at various depths, precipitation, and temperature. Applied Geography 34, 255–264. https://doi.org/10.1016/j.apgeog.2011.11.009

Malone, R.W., Ahuja, L.R., Ma, L., Don Wauchope, R., Ma, Q., Rojas, K.W., 2004. Application of the Root Zone Water Quality Model (RZWQM) to pesticide fate and transport: an overview. Pest Management Science: formerly Pesticide Science 60, 205–221.

Mironov, Bobrov, P.P., Fomin, S.V., 2014. Dielectric model of moist soils with varying clay content in the 0.04 to 26.5 GHz frequency range, in: 2013 International Siberian Conference on Control and Communications (SIBCON). Presented at the 2013 International Siberian Conference on Control and Communications (SIBCON 2013), IEEE, Krasnoyarsk, Russia, pp. 1–4. https://doi.org/10.1109/SIBCON.2013.6693613

Mironov, Bobrov, P.P., Fomin, S.V., 2013. Multirelaxation Generalized Refractive Mixing Dielectric Model of Moist Soils. IEEE Geosci. Remote Sensing Lett. 10, 603–606. https://doi.org/10.1109/LGRS.2012.2215574

Mishra, V., Cruise, J.F., Hain, C.R., Mecikalski, J.R., Anderson, M.C., 2018. Development of soil moisture profiles through coupled microwave–thermal infrared observations in the southeastern United States. Hydrol. Earth Syst. Sci. 22, 4935–4957. https://doi.org/10.5194/hess-22-4935-2018

Mishra, V., Ellenburg, W.L., Markert, K.N., Limaye, A.S., 2020. Performance evaluation of soil moisture profile estimation through entropy-based and exponential filter models. Hydrological Sciences Journal 65, 1036–1048. https://doi.org/10.1080/02626667.2020.1730846

Njoku, E.G., Kong, J.-A., 1977. Theory for passive microwave remote sensing of near-surface soil moisture. J. Geophys. Res. 82, 3108–3118. https://doi.org/10.1029/JB082i020p03108

Njoku, E.G., O'Neill, P.E., 1982. Multifrequency Microwave Radiometer Measurements of Soil Moisture. IEEE Trans. Geosci. Remote Sensing GE-20, 468–475. https://doi.org/10.1109/TGRS.1982.350412

Qiu, Y., Fu, B., Wang, J., Chen, L., Meng, Q., Zhang, Y., 2010. Spatial prediction of soil moisture content using multiple-linear regressions in a gully catchment of the Loess Plateau, China. Journal of Arid Environments 74, 208–220. https://doi.org/10.1016/j.jaridenv.2009.08.003

Rao, K.S., Chandra, G., Narasimha Rao, P.V., 1988. Study on penetration depth and its dependence on frequency, soil moisture, texture and temperature in the context of microwave remote sensing. J Indian Soc Remote Sens 16, 7–19. https://doi.org/10.1007/BF03014300

Reich, P.B., Sendall, K.M., Stefanski, A., Rich, R.L., Hobbie, S.E., Montgomery, R.A., 2018. Effects of climate warming on photosynthesis in boreal tree species depend on soil moisture. Nature 562, 263–267. https://doi.org/10.1038/s41586-018-0582-4

Reutov, E.A., Shutko, A.M., 1986. Prior-knowledge-based soil-moisture determination by microwave radiometry. Soviet Journal of Remote Sensing 5, 100–125.

Sabater, J.M., Jarlan, L., Calvet, J.-C., Bouyssel, F., De Rosnay, P., 2007. From Near-Surface to Root-Zone Soil Moisture Using Different Assimilation Techniques. J. Hydrometeor. 8, 194–206. https://doi.org/10.1175/JHM571.1

Sadeghi, M., Tabatabaeenejad, A., Tuller, M., Moghaddam, M., Jones, S., 2016. Advancing NASA's AirMOSS P-Band Radar Root Zone Soil Moisture Retrieval Algorithm via Incorporation of Richards' Equation. Remote Sensing 9, 17. https://doi.org/10.3390/rs9010017

Sadri, S., Pan, M., Wada, Y., Vergopolan, N., Sheffield, J., Famiglietti, J.S., Kerr, Y., Wood, E., 2020. A global near-real-time soil moisture index monitor for food security using integrated SMOS and SMAP. Remote Sensing of Environment 246, 111864. https://doi.org/10.1016/j.rse.2020.111864

Schmugge, T.J., Choudhury, B.J., 1981. A comparison of radiative transfer models for predicting the microwave emission from soils. Radio Sci. 16, 927–938. https://doi.org/10.1029/RS016i005p00927

Seneviratne, S.I., Corti, T., Davin, E.L., Hirschi, M., Jaeger, E.B., Lehner, I., Orlowsky, B., Teuling, A.J., 2010. Investigating soil moisture–climate interactions in a changing climate: A review. Earth-Science Reviews 99, 125–161.

Shen, X., Walker, J.P., Ye, N., Wu, X., Boopathi, N., Yeo, I.-Y., Zhang, L., Zhu, L., 2020. Soil Moisture Retrieval Depth of P- and L-Band Radiometry: Predictions and Observations. IEEE Trans. Geosci. Remote Sensing 1–9. https://doi.org/10.1109/TGRS.2020.3026384

Shen, X., Walker, J.P., Ye, N., Wu, X., Brakhasi, F., Boopathi, N., Zhu, L., Yeo, I.-Y., Kim, E., Kerr, Y., Jackson, T., 2022a. Evaluation of the tau-omega model over bare and wheat-covered flat and periodic soil surfaces at P- and L-band. Remote Sensing of Environment 273, 112960. https://doi.org/10.1016/j.rse.2022.112960

Shen, X., Walker, J.P., Ye, N., Wu, X., Brakhasi, F., Boopathi, N., Zhu, L., Yeo, I.-Y., Kim, E., Kerr, Y., Jackson, T., 2022b. Impact of random and periodic surface roughness on P- and L-band radiometry. Remote Sensing of Environment 269, 112825. https://doi.org/10.1016/j.rse.2021.112825

Shi, Y., Wu, P., Zhao, X., Li, H., Wang, J., Zhang, B., 2014. Statistical analyses and controls of root-zone soil moisture in a large gully of the Loess Plateau. Environ Earth Sci 71, 4801–4809. https://doi.org/10.1007/s12665-013-2870-5

Stogryn, A., 1970. The Brightness Temperature of a Vertically Structured Medium. Radio Sci. 5, 1397–1406. https://doi.org/10.1029/RS005i012p01397

Tabatabaeenejad, A., Burgin, M., Duan, X., Moghaddam, M., 2013. Airborne Microwave Observatory of Subcanopy and Subsurface radar retrieval of root zone soil moisture: Preliminary results, in: 2013 IEEE Radar Conference (RadarCon13). Presented at the 2013 IEEE Radar Conference (RadarCon), IEEE, Ottawa, ON, Canada, pp. 1–4. https://doi.org/10.1109/RADAR.2013.6586082

Tabatabaeenejad, A., Burgin, M., Xueyang Duan, Moghaddam, M., 2015. P-Band Radar Retrieval of Subsurface Soil Moisture Profile as a Second-Order Polynomial: First AirMOSS Results. IEEE Trans. Geosci. Remote Sensing 53, 645–658. https://doi.org/10.1109/TGRS.2014.2326839

Tabatabaeenejad, A., Chen, R.H., Moghaddam, M., 2016. Assessment of retrieval errors of AirMOSS root-zone soil moisture products, in: 2016 IEEE International Geoscience and Remote Sensing Symposium (IGARSS). Presented at the IGARSS 2016 - 2016 IEEE International Geoscience and Remote Sensing Symposium, IEEE, Beijing, China, pp. 5268–5271. https://doi.org/10.1109/IGARSS.2016.7730372

Tabatabaeenejad, A., Sadeghi, M., Moghaddam, M., Tuller, M., Jones, S.B., 2017. Retrieval of AirMOSS root-zone soil moisture profile with a richards' equation-based approach, in: 2017 IEEE International Geoscience and Remote Sensing Symposium (IGARSS). Presented at the 2017 IEEE International Geoscience and Remote Sensing Symposium (IGARSS), IEEE, Fort Worth, TX, pp. 4955–4958. https://doi.org/10.1109/IGARSS.2017.8128116

Tsang, L., Njoku, E., Kong, J.A., 1975. Microwave thermal emission from a stratified medium with nonuniform temperature distribution. Journal of Applied Physics 46, 5127–5133. https://doi.org/10.1063/1.321571

Ulaby, F.T., Long, D.G., 2014. Microwave radar and radiometric remote sensing. The University of Michigan Press, Ann Arbor.

Walker, J.P., Willgoose, G.R., Kalma, J.D., 2001. One-Dimensional Soil Moisture Profile Retrieval by Assimilation of Near-Surface Measurements: A Simplified Soil Moisture Model and Field Application. JOURNAL OF HYDROMETEOROLOGY 2, 18.

Wang, J.R., Choudhury, B.J., 1981. Remote sensing of soil moisture content, over bare field at 1.4 GHz frequency 27.

Wigneron, J.-P., Laguerre, L., Kerr, Y.H., 2001. A simple parameterization of the L-band microwave emission from rough agricultural soils. IEEE Trans. Geosci. Remote Sensing 39, 1697–1707. https://doi.org/10.1109/36.942548

Wilheit, T.T., 1978. Radiative Transfer in a Plane Stratified Dielectric. IEEE Trans. Geosci. Electron. 16, 138–143. https://doi.org/10.1109/TGE.1978.294577

Xia, Y., Watts, J.D., Machmuller, M.B., Sanderman, J., 2022. Machine learning based estimation of field-scale daily, high resolution, multi-depth soil moisture for the Western and Midwestern United States. PeerJ 10, e14275. https://doi.org/10.7717/peerj.14275

Xu, L., Chen, N., Zhang, X., Moradkhani, H., Zhang, C., Hu, C., 2021. In-situ and triple-collocation based evaluations of eight global root zone soil moisture products. Remote Sensing of Environment 254, 112248. https://doi.org/10.1016/j.rse.2020.112248

Yi, Y., Chen, R.H., Nicolsky, D., Moghaddam, M., Kimball, J.S., Romanovsky, V.E., Miller, C.E., 2019. Developing A Soil Inversion Model Framework for Regional Permafrost Monitoring, in: IGARSS 2019 - 2019 IEEE International Geoscience and Remote Sensing Symposium. Presented at the IGARSS 2019 - 2019 IEEE International Geoscience and Remote Sensing Symposium, IEEE, Yokohama, Japan, pp. 4032–4035. https://doi.org/10.1109/IGARSS.2019.8898856

Yuan, S., Quiring, S.M., Zhao, C., 2020. Evaluating the Utility of Drought Indices as Soil Moisture Proxies for Drought Monitoring and Land–Atmosphere Interactions. Journal of Hydrometeorology 21, 2157–2175. https://doi.org/10.1175/JHM-D-20-0022.1

Yueh, S., Shah, R., Xu, X., Elder, K., Starr, B., 2020. Experimental Demonstration of Soil Moisture Remote Sensing Using P-Band Satellite Signals of Opportunity. IEEE Geosci. Remote Sensing Lett. 17, 207–211. https://doi.org/10.1109/LGRS.2019.2918764

Zhang, K., Ali, A., Antonarakis, A., Moghaddam, M., Saatchi, S., Tabatabaeenejad, A., Chen, R., Jaruwatanadilok, S., Cuenca, R., Crow, W.T., Moorcroft, P., 2019. The Sensitivity of North American Terrestrial Carbon Fluxes to Spatial and Temporal Variation in Soil Moisture: An Analysis Using Radar-Derived Estimates of Root-Zone Soil Moisture. J. Geophys. Res. Biogeosci. 124, 3208–3231. https://doi.org/10.1029/2018JG004589

Zhang, L., Meng, Q., Hu, D., Zhang, Y., Yao, S., Chen, X., 2020. Comparison of different soil dielectric models for microwave soil moisture retrievals. International Journal of Remote Sensing 41, 3054–3069. https://doi.org/10.1080/01431161.2019.1698077

Zheng, D., Li, X., Wang, X., Wang, Z., Wen, J., van der Velde, R., Schwank, M., Su, Z., 2019. Sampling depth of L-band radiometer measurements of soil moisture and freeze-thaw dynamics on the Tibetan Plateau. Remote Sensing of Environment 226, 16–25. https://doi.org/10.1016/j.rse.2019.03.029

Zhou, X., Lei, W., Ma, J., 2016. Entropy Base Estimation of Moisture Content of the Top 10-m Unsaturated Soil for the Badain Jaran Desert in Northwestern China. Entropy 18, 323. https://doi.org/10.3390/e18090323

Highlights:

1- **Combined L&P-band radiometry outperformed using either band alone.**
2- **Second -order polynomial found best for soil moisture profile retrieval.**
3- **Soil moisture profile retrieval via time series outperformed snapshot retrieval.**

Declaration of interests

☒ The authors declare that they have no known competing financial interests or personal relationships that could have appeared to influence the work reported in this paper.

☐ The authors declare the following financial interests/personal relationships which may be considered as potential competing interests: